

Article

Geochemical Characteristics and Constraints on Provenance, Tectonic Setting, and Paleoweathering of Middle Jurassic Zhiluo Formation Sandstones in the Northwest Ordos Basin, North-Central China

Yelei Cai ¹, Fei Ouyang ^{1,*}, Xianrong Luo ¹, Zilong Zhang ², Meilan Wen ¹, Xiaoneng Luo ² and Rui Tang ¹

¹ College of Earth Science, Guilin University of Technology, Guilin 541004, China; caiyelei1228@126.com (Y.C.); lxr811@glut.edu.cn (X.L.); mlwen@glut.edu.cn (M.W.); 15308383616@163.com (R.T.)

² Beijing Research Institute of Uranium Geology, China National Nuclear Corporation, Beijing 100029, China; zhangzilong@briug.cn (Z.Z.); lxnabriug@126.com (X.L.)

* Correspondence: ouyf@glut.edu.cn

Abstract: To further explore the uranium-bearing prospects of the Zhiluo Formation, the petrography, major elements, trace elements and rare earth elements of Zhiluo sandstone samples collected from four boreholes were analyzed in this research to determine the provenance, tectonic setting and paleoweathering of the formation. The results of the analysis reveal that the Zhiluo Formation sandstone comprises primarily feldspar sandstone, with quartz, feldspar, and mica as the main mineral components. The rare earth elements are mainly characterized by enrichment in light rare earth elements and loss of heavy rare earth elements. The ratio of light to heavy rare earth elements (LREEs/HREEs) is 5.55–7.79, with an average of 6.33. The value of $(La/Yb)_{CN}$ is 12.96–22.33, with an average value of 17.41, indicating obvious fractionation of LREEs and HREEs. The chemical index of alteration (CIA) value of this sandstone is 56.30–63.04, with an average of 59.75, which indicates that the parent rock experienced weak chemical weathering in a dry climate. The discrimination diagrams of the source area and parent rock show that the source area of the Zhiluo sandstones had a mixed intermediate-felsic composition, and that the main parent rocks were andesite and granite. The tectonic setting discrimination diagram indicates that the tectonic setting of the source area was the passive margin. Thus, the provenance of the sandstone of the Zhiluo Formation is proposed to be the volcanic-sedimentary rock series developed on the northern margin of the Ordos Basin.

Keywords: geochemical characteristics; source area; tectonic setting; Zhiluo Formation; Bayinqinggeli sandstone-type uranium deposit; Ordos Basin



Citation: Cai, Y.; Ouyang, F.; Luo, X.; Zhang, Z.; Wen, M.; Luo, X.; Tang, R. Geochemical Characteristics and Constraints on Provenance, Tectonic Setting, and Paleoweathering of Middle Jurassic Zhiluo Formation Sandstones in the Northwest Ordos Basin, North-Central China. *Minerals* **2022**, *12*, 603. <https://doi.org/10.3390/min12050603>

Academic Editors: Jianghai Yang and Georgia Pe-Piper

Received: 6 April 2022

Accepted: 4 May 2022

Published: 10 May 2022

Publisher's Note: MDPI stays neutral with regard to jurisdictional claims in published maps and institutional affiliations.



Copyright: © 2022 by the authors. Licensee MDPI, Basel, Switzerland. This article is an open access article distributed under the terms and conditions of the Creative Commons Attribution (CC BY) license (<https://creativecommons.org/licenses/by/4.0/>).

1. Introduction

Provenance analysis is particularly significant for elucidating the genesis and distribution features of sedimentary formations in a basin, as well as for reconstructing the tectonic setting of the source area, the sediment transport route, and the filling history of the sedimentary basin [1–5]. The clastic and geochemical compositions of sandstones are largely controlled by the provenance area, and these compositions also retain relevant information about the parent rock and tectonic setting [6–11]. In recent years, mineralogical, petrographical, and geochemical methods have been extensively employed to identify the provenance, tectonic setting, and paleoweathering of provenance areas, with remarkable results offering new evidence for understanding the evolution of the basin [12–15].

Uranium is a strategic resource closely related to national security and economic development. Uranium resources are an important guarantee for the sustainable development of nuclear energy and national defense construction in China. In order to ensure sustainable economic development and ecological civilization construction in China, nuclear energy, as one of the clean energy sources, is of great significance for adjusting and optimizing

the energy structure of China, improving the ecological environment and reducing CO₂ and S emissions. Sandstone-type uranium deposits play an important role in the supply of uranium resources in China. They are characterized by shallow depth, large-scale reserves, low cost of mining and environmental friendliness [16]. The Ordos Basin is one of the important uranium-bearing basins in China, and its northern part is the major ore concentration area of sandstone-type uranium deposits. In recent years, many sandstone-type uranium deposits have been reported from the northern Ordos Basin; Zaohuohao, Nalinggou, Daying, Hangjinqi and Bayinqinggeli uranium deposits have been gradually discovered. The Bayinqinggeli region, located in the northern Ordos Basin, is one of the primary areas for uranium exploration in the basin. Industrialized uranium ore bodies have been discovered in the Zhiluo Formation in Bayinqinggeli. Previous studies in this area have mainly focused on geological structure, sedimentary characteristics [17], fluid characteristics [18], metallogenic models [19] and ore-controlling factors [16] of sandstone-type uranium deposits, but research on the provenance of the Zhiluo Formation sandstone and tectonic setting of the provenance area is relatively lacking [20–24]. Provenance research on uranium-bearing formations can provide certain constraints for determining the source of uranium minerals, which has become a current research hotspot and focus [22,25–27]. The provenance system can provide an accurate record of information about regional tectonic evolution, and research on the characteristics of the provenance area can further infer the overall sedimentary tectonic setting in the area and then guide the next step of uranium exploration work.

This research discusses mainly the provenance, tectonic setting, paleoweathering and paleoclimatic conditions of the Zhiluo Formation sandstone through a comprehensive study of the petrographic and geological characteristics of this lithostratigraphic unit in the Bayinqinggeli area. This study has important theoretical and practical significance for confirming the provenance of uranium-bearing strata, pointing out the direction for further ore prospecting in this area, and reconstructing the paleoclimatic and paleogeographic evolution of the Zhiluo Formation in the northern Ordos Basin.

2. Geological Setting

The Ordos Basin is a polycyclic superimposed basin that is located in the west of the North China Platform, it has a rectangular shape, extending from north to south. It can be divided into six tectonic units that include the Yimeng uplift, Yishan slope, Jinxi flexural fold belt, Tianhuan depression, western margin thrust belt and Weibei uplift [18]. The overall tectonic pattern of the basin is tectonic belts with different characteristics developed along the basin margin, while the internal tectonic of the basin is relatively undeveloped. The Ordos Basin is surrounded by orogenic belts, which include the Yinshan orogenic belt to the north, the Qinling orogenic belt to the south, Helan Mountain to the west and Taihang Mountain to the east (Figure 1a) [19]. The basin began to deposit stably in the Mesoproterozoic and progressively split from the North China Basin, which evolved into a stable cratonic basin, and subsequently continued to deposited stably. The basin contains two basement units, one of them is direct, and the other is indirect, with the characteristics of “double” basement. Archean-Palaeoproterozoic metamorphic rock series form an indirect basement unit, while the direct basement unit is the platform sedimentary cover of Paleoproterozoic-Mesozoic Triassic. The Triassic (T), Jurassic (J), Lower Cretaceous (K₁), Paleogene (E₃), Neogene (N₂) and Quaternary (Q) sedimentary bodies span the basin, where the Jurassic and Lower Cretaceous are the dominant sedimentary units.

The Bayinqinggeli area is located in the northern Ordos Basin, northwest of the Daying mining area. The sand body of the Zhiluo Formation is well developed and has good uranium metallogenic conditions [21]. The Zhiluo Formation can be divided into upper and lower members, the upper member is dominated by flood deposits, and the sand body is relatively undeveloped, formed by a set of primary red clastic; the lower member is a developed sand body of fluvial facie and dominated by primary grey clastic rocks. In

the study region, the major exposed strata are Quaternary (Q) and Lower Cretaceous (K₁), while a small area of Middle Triassic (T₂) is exposed in the east (Figure 1b).

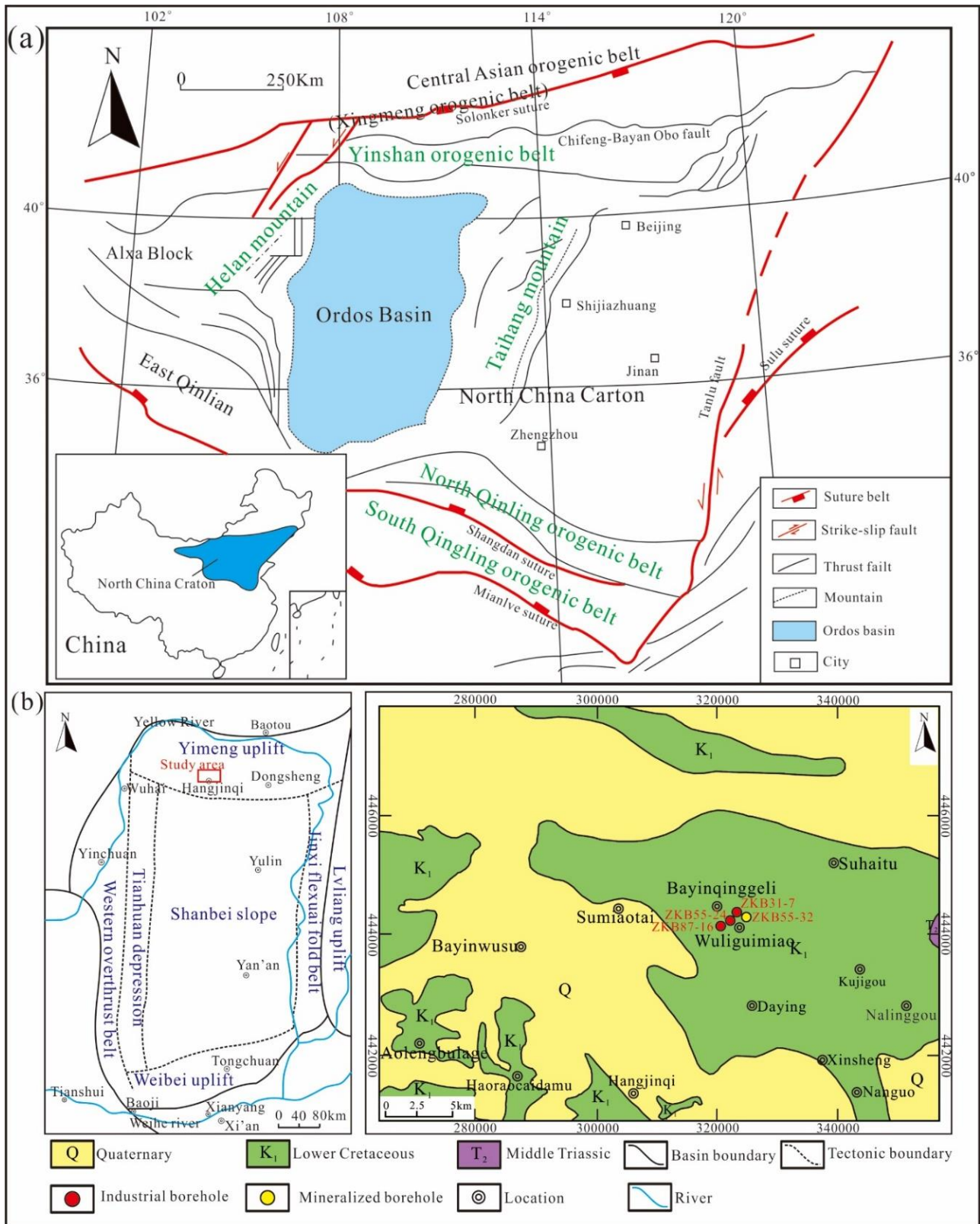


Figure 1. Map of the research area: (a) Simplified geological map of North-Central China [28]; (b) the division of tectonic units in Ordos Basin and Regional geological map of research area.

3. Materials and Methods

The 21 Zhiluo Formation sandstone samples in this research were collected from the ZKB31-7, ZKB55-32, ZKB55-24 and ZKB87-16 boreholes in the Bayinqinggeli area, northwestern Ordos Basin (Figure 2). All samples are medium and fine sandstone. When sampling, sandstone samples with low radioactivity were selected to ensure the accuracy and representativeness of the analysis, and the drilling fluid was removed from the sandstone surface. The major, trace and rare earth element (REE) analyses of the samples were completed in the Analytical Laboratory of Beijing Research Institute of Uranium Geology (Beijing, China).

Before chemical analysis, the sample was crushed in an agate mortar to 200 mesh. The analysis and determination method was as follows: the major element analysis was determined with an XRF-1800 fluorescence spectrometer, the accuracy of which was better than 1%. The test voltage was 50 kV, the current was 50 mA, and the loss on ignition (LOI) was estimated by firing the dried sample at 1000 °C for two hours and then measuring the weight loss.

Trace elements and rare earth elements (REEs) were tested by inductively coupled plasma-mass spectrometry (ICP-MS) (PerkinElmer, Waltham, MA, USA). The accuracy was better than 5%. We accurately weighed out 25 mg powder samples, placed them into the inner tank of the closed sample dissolver, added hydrofluoric (HF) and nitric acid (HNO₃) and sealed the tank. The sample dissolver was placed in the oven and heated at 185 °C for 2 h. After cooling, each sample was heated and dried on an electric heating plate, and HNO₃ was then repeatedly added to assist in drying. Finally, HNO₃ was added, and the sample was again sealed, placed in an oven, heated at 130 °C for 3 h, cooled, diluted with water and analyzed by ICP-MS.

Paleoweathering of the source area was qualitatively evaluated by the following chemical indices; chemical index of alteration (CIA) = $\text{Al}_2\text{O}_3 / (\text{Al}_2\text{O}_3 + \text{CaO}^* + \text{Na}_2\text{O} + \text{K}_2\text{O}) \times 100$, the index of compositional variability (ICV) = $(\text{Fe}_2\text{O}_3 + \text{K}_2\text{O} + \text{Na}_2\text{O} + \text{CaO}^* + \text{MgO} + \text{MnO} + \text{TiO}_2) / \text{Al}_2\text{O}_3$ [19] and the plagioclase index of alteration (PIA) = $(\text{Al}_2\text{O}_3 - \text{K}_2\text{O}) / (\text{Al}_2\text{O}_3 + \text{CaO}^* + \text{Na}_2\text{O} - \text{K}_2\text{O}) \times 100$ [20]. In the formulas above, all parameters were calculated using the percentage of oxide, except for the ICV, as the calculation of ICV is based on the mole percentages of all oxides, and CaO* refers to only the mole percentage of CaO in silicate minerals. The CaO content in the samples varied widely due to the instability of silicate minerals [11,20]. Calculating the value of CIA with the total CaO could lead to false conclusions. Therefore, the correction method of CaO* was as follows: first, the CaO in apatite is removed by P₂O₅, that is, $\text{CaO}^{**} = \text{mol CaO} - (10/3 \times \text{mol P}_2\text{O}_5)$, resulting in CaO**, and then mol Na₂O is calculated and compared. If $\text{CaO}^{**} > \text{Na}_2\text{O}$, then $\text{mol CaO}^* = \text{mol Na}_2\text{O}$, otherwise, $\text{mol CaO}^* = \text{mol CaO}$ [10].

The discrimination diagrams based on major elements were used to distinguish the provenance of the sandstone samples from the Zhiluo Formation. In addition, the discrimination diagrams based on major and trace elements were used to assess the tectonic setting of the sandstone samples from the Zhiluo Formation.

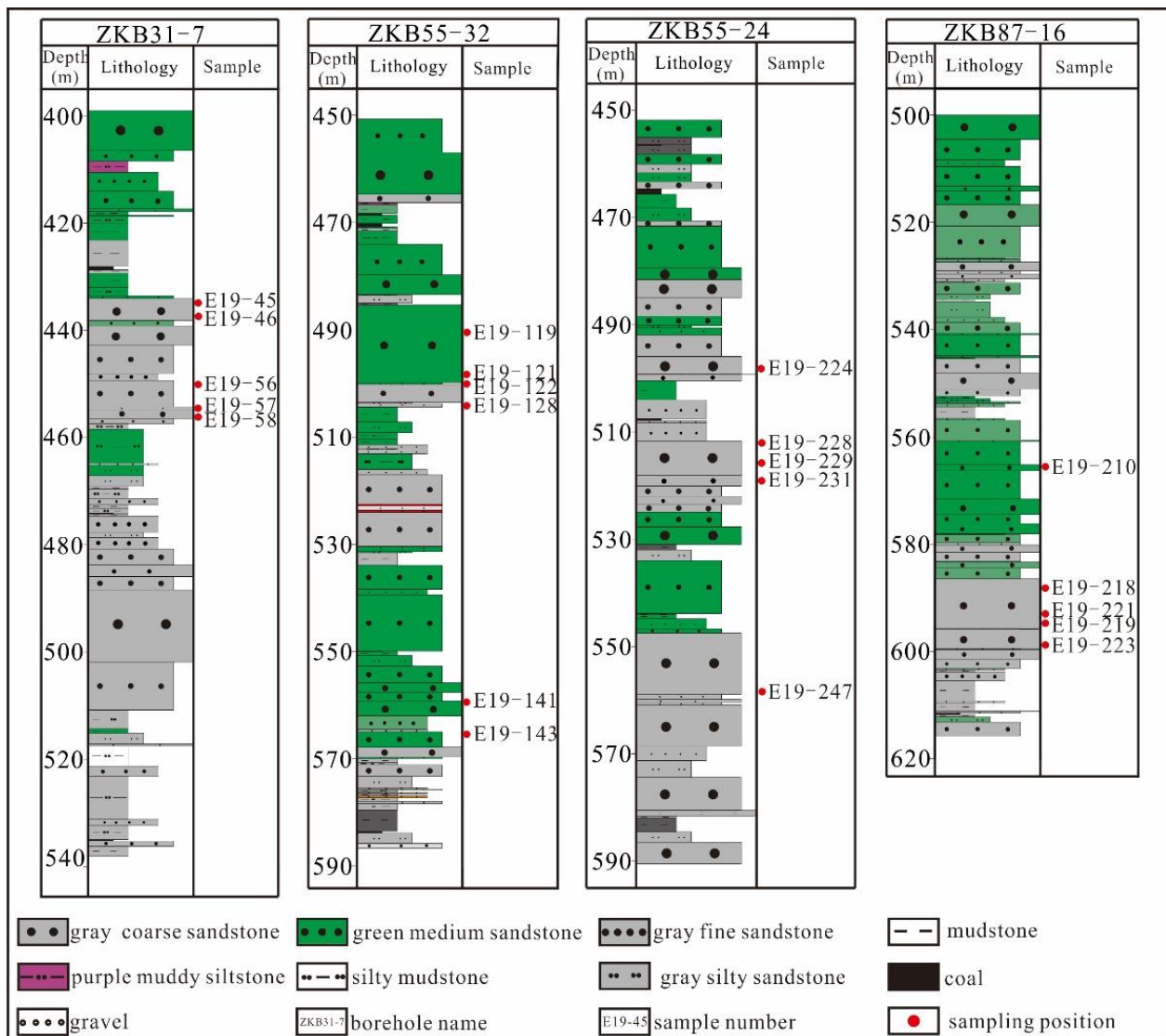


Figure 2. Drilling sampling map of the study area.

4. Geochemical Results

4.1. Petrography of Sandstones

A petrological identification of representative sandstone samples from the Zhiluo Formation was carried out. The Zhiluo Formation sandstones are feldspathic litharenite and lithic arkose, mainly composed of quartz, feldspar, debris, and mica. The quartz is mono-crystalline quartz, which is brilliant with equant forms and moderately undulous extinction. The majority of the quartz grains have a secondary growth along the edges. The feldspar crystals include plagioclase, orthoclase, and microplagioclase. The mica includes biotite and muscovite, which is striped or angular, but the majority of the mica is biotite (Figure 3).

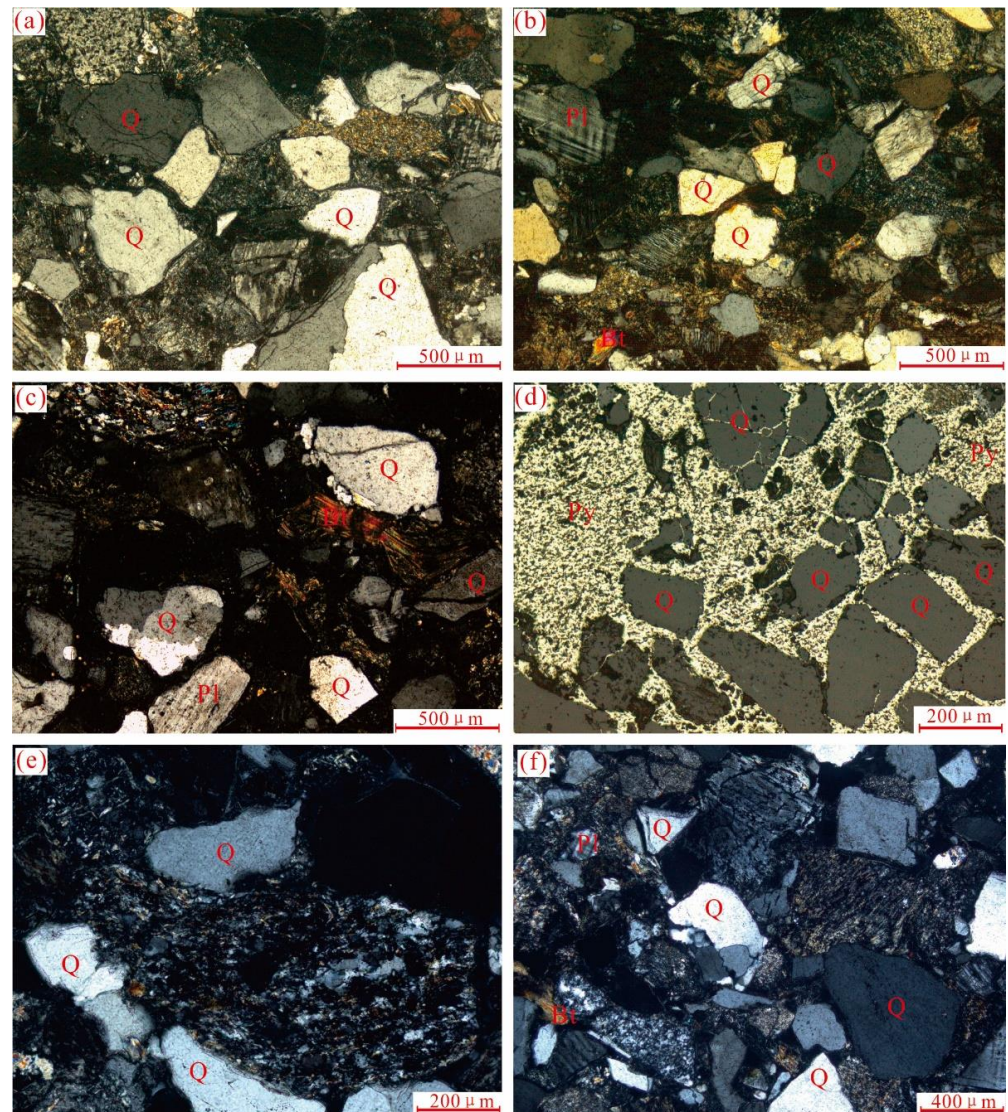


Figure 3. Photomicrograph of the Zhiluo Formation sandstones. (a) Quartz particles with secondary enlargement edge, complex clastic composition, pore-contact cementation; (b) mica flakes are strongly curved; (c) hydromicization of some plagioclases and deformation structure of biotite; (d) pyrite cementation debris containing disseminated fine-grained pyrite; (e) Metamorphic rock debris can be clearly seen, and some quartz particles have secondary enlarged edges; (f) contact cementation. All photomicrographs were taken using cross-polarized light; Q, quartz; Pl, plagioclase; Py, pyrite; Bi, biotite.

4.2. Major Element Geochemistry

Major element content data for the sandstone samples are listed in Table 1. In all the studied samples, SiO₂ (68.91~74.83%, average 72.04%) is the prevalent oxide, and Al₂O₃ (11.77~14.12%, average 12.60%) content has a wide range. The contents of other major elements are as follows: CaO (0.62~1.84%, average 1.02%), MgO (0.87~1.57%, average 1.17%), K₂O (3.04~3.51%, average 3.25%), Na₂O (1.25~2.90%, average 2.07%), TiO₂ (0.29~0.85%, average 0.47%), and Fe₂O₃^T (1.54~3.19%, average 2.29%). The Zhiluo sandstone is characterized by low MnO (0.02~0.06%, average 0.03%) and P₂O₅ (0.08~0.13%, average 0.10%).

Table 1. Major oxide concentration in wt% of sandstones from the Zhiluo Formation.

Sample No.	SiO ₂	TiO ₂	Al ₂ O ₃	Fe ₂ O ₃ ^T	FeO	MgO	CaO	Na ₂ O	K ₂ O	MnO	P ₂ O ₅	LOI	CaO*	ICV	CIA	PIA	SiO ₂ /Al ₂ O ₃	K ₂ O/Na ₂ O	Fe ₂ O ₃ ^T + MgO
E19-45	74.83	0.29	12.42	1.54	1.10	0.78	0.97	2.90	3.04	0.02	0.08	3.10	0.89	0.77	56.34	59.04	6.02	1.05	2.39
E19-58	72.61	0.41	12.76	1.84	1.44	1.06	1.01	2.42	3.27	0.03	0.09	4.45	0.94	0.79	58.24	62.17	5.69	1.35	3.04
E19-57	73.69	0.43	12.36	1.69	1.18	0.83	1.12	2.44	3.45	0.04	0.08	3.77	1.06	0.81	56.30	59.55	5.96	1.41	2.62
E19-56	72.71	0.40	12.84	1.88	1.25	0.96	1.02	2.52	3.48	0.03	0.08	4.02	0.95	0.80	57.31	61.01	5.66	1.38	2.96
E19-46	72.27	0.58	12.85	2.32	1.40	1.00	1.01	2.62	3.08	0.04	0.10	4.11	0.92	0.83	58.17	61.70	5.62	1.18	3.46
E19-247	71.66	0.37	12.93	2.45	1.49	1.16	0.62	2.04	3.51	0.03	0.09	4.59	0.53	0.79	61.56	68.11	5.54	1.72	3.81
E19-229	73.69	0.54	12.10	2.43	1.55	0.97	0.83	2.23	3.32	0.04	0.08	3.76	0.75	0.86	58.51	63.05	6.09	1.49	3.53
E19-224	69.62	0.55	14.12	2.92	2.53	1.33	0.81	2.34	3.44	0.03	0.10	4.67	0.71	0.81	61.62	67.22	4.93	1.47	4.46
E19-231	74.16	0.48	11.77	2.40	1.55	1.05	0.85	2.27	3.12	0.04	0.10	3.69	0.75	0.87	58.26	62.42	6.30	1.37	3.59
E19-228	73.58	0.39	12.41	2.05	1.43	0.93	0.75	2.28	3.34	0.03	0.08	4.08	0.67	0.79	59.25	64.12	5.93	1.46	3.10
E19-121	71.84	0.50	12.06	2.54	1.53	1.47	0.87	1.46	3.05	0.03	0.09	6.02	0.80	0.82	63.04	69.92	5.96	2.09	4.27
E19-141	71.76	0.35	12.01	2.16	1.52	1.31	1.66	1.78	3.18	0.04	0.09	5.65	1.64	0.87	56.68	59.89	5.98	1.79	3.68
E19-119	70.42	0.44	12.11	2.34	1.34	1.49	1.84	1.45	3.07	0.03	0.09	6.65	1.41	0.88	59.94	64.81	5.82	2.12	4.11
E19-122	71.37	0.48	12.61	2.60	1.64	1.40	0.83	1.77	3.17	0.04	0.09	5.58	0.76	0.82	62.25	68.52	5.66	1.79	4.24
E19-143	69.50	0.50	13.26	2.79	1.91	1.57	1.10	1.72	3.12	0.04	0.11	6.20	1.01	0.82	62.57	68.44	5.24	1.81	4.65
E19-128	71.73	0.75	12.46	2.72	2.21	1.10	1.10	2.38	3.11	0.06	0.09	4.43	1.03	0.90	57.88	61.46	5.76	1.31	4.00
E19-210	70.80	0.36	12.32	2.02	1.42	1.41	1.55	1.25	3.32	0.04	0.08	6.83	1.21	0.81	61.52	67.97	5.75	2.66	3.68
E19-218	72.68	0.35	12.35	1.93	1.14	1.08	0.97	1.76	3.26	0.03	0.09	5.40	0.90	0.76	60.77	66.50	5.89	1.85	3.19
E19-223	72.46	0.36	12.77	2.13	1.28	1.16	0.67	1.85	3.32	0.02	0.09	5.13	0.59	0.74	62.55	69.37	5.67	1.79	3.47
E19-221	72.53	0.41	12.83	2.16	1.39	1.13	0.65	1.98	3.31	0.02	0.08	4.88	0.56	0.75	62.15	68.61	5.65	1.67	3.46
E19-219	68.91	0.85	13.12	3.19	1.71	1.35	1.29	1.95	3.33	0.04	0.13	5.82	1.19	0.91	59.74	64.50	5.25	1.71	4.82
Average	72.04	0.47	12.59	2.29	1.52	1.17	1.02	2.07	3.25	0.03	0.09	4.90	0.92	0.82	59.75	64.68	5.73	1.64	3.64
UCC	66.62	0.64	15.40	5.04	–	2.48	2.59	3.27	2.80	0.10	0.15	–	–	–	52.74	–	4.32	0.86	7.52

UCC: Upper continental crust, quoted in Rudnick and Gao. Fe₂O₃^T: total Fe expressed as Fe₂O₃. LOI: loss on ignition; ICV: index of compositional variability; CIA: chemical index of alteration; PIA: plagioclase index of alteration.

The concentrations of major elements are often used for the geochemical classification of sandstone [29,30]. The SiO_2 content and $\text{SiO}_2/\text{Al}_2\text{O}_3$ ratio are common geochemical standards for determining the maturity of sediments and reflect the contents of quartz, clay and feldspar in sedimentary rocks. In addition, the sum of $\text{Na}_2\text{O} + \text{K}_2\text{O}$ reflects the feldspar content and is used to determine the chemical maturity of sediments [31]. The Zhiluo Formation sandstone samples have the characteristics of low $\text{Al}_2\text{O}_3/\text{SiO}_2$ ratio, low $\text{K}_2\text{O}/\text{Na}_2\text{O}$ ratio and high $\text{K}_2\text{O}/\text{Na}_2\text{O}$ ratio. The bivariate diagram of $\log(\text{Fe}_2\text{O}_3/\text{K}_2\text{O})$ versus $\log(\text{SiO}_2/\text{Al}_2\text{O}_3)$ [32] indicates that the majority of the samples plot in the arkose field. Additionally, there are few samples distributed within the wacke area (Figure 4). These results show that the maturity of the Zhiluo Formation sandstones in the Bayinqingeli area is low.

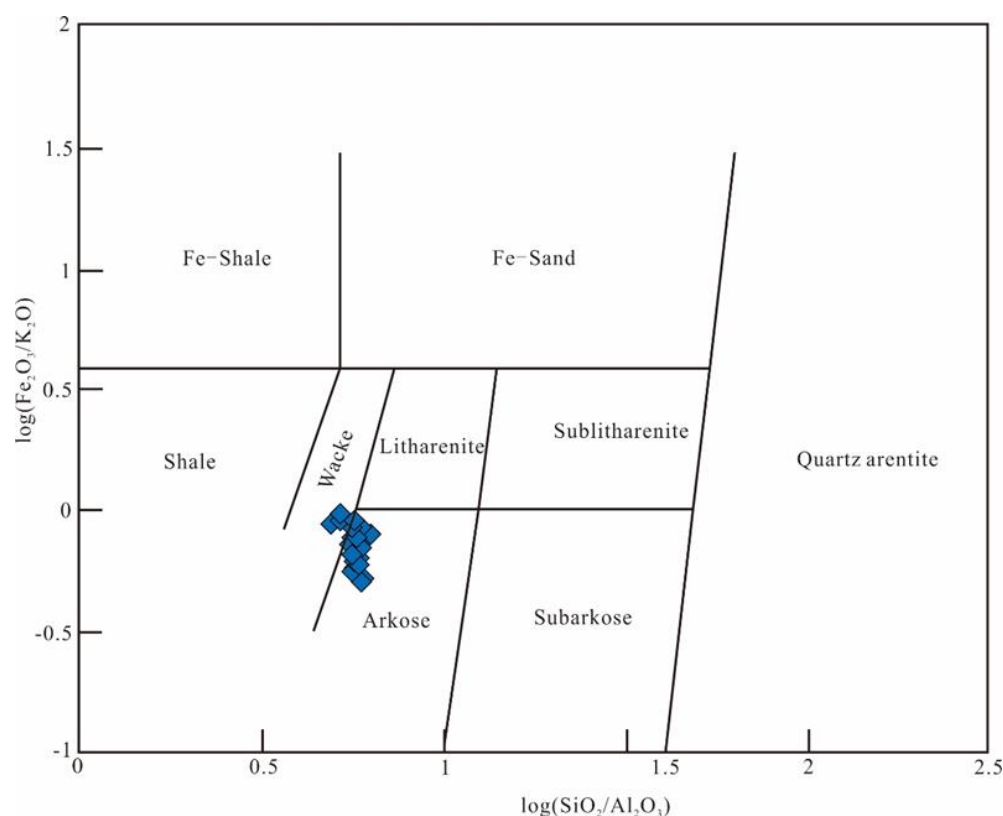


Figure 4. Geochemical classification diagram [32] of $\log(\text{Fe}_2\text{O}_3/\text{K}_2\text{O})$ plotted against $\log(\text{SiO}_2/\text{Al}_2\text{O}_3)$ for sandstones from the Zhiluo Formation.

4.3. Trace Element Geochemistry

The trace element content data for the sandstones are presented in Table 2. In general, the trace element concentrations of sandstones have wide ranges. Some high-field strength elements are difficult to dissolve and have strong stability during transportation and deposition, such as Hf (0.96~3.09 ppm, average 1.40 ppm), Zr (30.5~160 ppm, average 44.48 ppm) and Ni (5.38~21.00 ppm, average 10.00 ppm). Therefore, these elements are often used to indicate the geochemical characteristics of the parent rock and the characteristics of the source area.

Table 2. Trace element concentrations (ppm) of sandstones from the Zhiluo Formation.

Sample No.	Rb	Sr	Ba	Pb	Th	U	Zr	Hf	Y	Sc	V	Cr	Cu	Co	Ni	Zn	Sc/Cr	Co/Th	Cr/Th	Th/Sc	Zr/Sc
E19-45	70.40	329.00	1025.00	12.10	3.57	6.84	30.80	1.03	8.89	6.54	34.00	31.10	6.56	6.51	10.40	31.30	0.21	1.82	8.71	0.55	4.71
E19-58	85.50	324.00	970.00	12.40	5.19	8.44	43.70	1.40	10.00	8.13	40.70	39.30	6.79	6.28	9.12	45.80	0.21	1.21	7.57	0.64	5.38
E19-57	82.90	312.00	1127.00	13.40	6.17	15.80	39.30	1.29	9.82	6.03	35.90	31.60	6.16	5.37	9.46	30.40	0.19	0.87	5.12	1.02	6.52
E19-56	88.20	314.00	1124.00	13.70	4.57	16.40	48.80	1.53	9.28	7.28	41.70	35.80	6.44	7.11	11.30	45.60	0.20	1.56	7.83	0.63	6.70
E19-46	76.00	333.00	952.00	17.20	4.50	17.30	41.00	1.36	10.80	8.72	47.30	48.10	9.29	8.04	14.00	46.20	0.18	1.79	10.69	0.52	4.70
E19-247	86.80	302.00	1105.00	12.10	4.09	8.15	41.80	1.32	8.21	6.42	46.50	35.10	8.93	6.41	11.10	41.30	0.18	1.57	8.58	0.64	6.51
E19-229	81.30	291.00	1005.00	12.10	5.32	13.60	40.20	1.27	9.36	7.00	50.80	39.20	6.90	6.68	10.20	40.70	0.18	1.26	7.37	0.76	5.74
E19-224	101.00	295.00	943.00	11.60	6.98	14.00	42.40	1.44	10.60	11.20	67.00	57.00	9.86	8.66	14.60	72.30	0.20	1.24	8.17	0.62	3.79
E19-231	74.20	276.00	972.00	10.80	4.40	14.60	37.60	1.17	9.51	6.56	46.20	40.20	7.21	5.59	9.25	53.30	0.16	1.27	9.14	0.67	5.73
E19-228	84.40	310.00	1035.00	11.70	4.16	16.70	30.80	0.96	8.62	7.19	50.90	40.00	6.70	7.49	10.60	49.80	0.18	1.80	9.62	0.58	4.28
E19-121	74.00	355.00	1025.00	11.60	5.51	2.33	34.30	1.14	9.27	7.18	47.20	40.10	7.68	8.31	12.90	46.10	0.18	1.51	7.28	0.77	4.78
E19-141	73.00	310.00	1123.00	10.80	3.79	2.91	41.40	1.25	7.58	5.79	143.00	30.10	8.32	5.69	10.90	34.00	0.19	1.50	7.94	0.65	7.15
E19-119	74.70	395.00	937.00	13.40	10.50	4.96	82.80	2.53	16.90	10.50	96.40	79.80	17.00	6.47	11.40	78.50	0.13	0.62	7.60	1.00	7.89
E19-122	85.10	359.00	1052.00	14.30	12.50	13.80	44.00	1.35	8.61	7.60	89.00	43.10	12.20	6.95	12.70	51.30	0.18	0.56	3.45	1.64	5.79
E19-143	80.00	316.00	1003.00	14.10	4.94	15.00	51.10	1.47	9.32	8.61	209.00	51.00	17.50	14.30	18.40	52.80	0.17	2.89	10.32	0.57	5.93
E19-128	74.50	325.00	1005.00	11.60	6.00	17.70	38.50	1.14	11.20	8.15	70.50	44.00	7.83	5.37	8.80	52.90	0.19	0.90	7.33	0.74	4.72
E19-210	92.00	331.00	1017.00	25.80	4.71	2.19	30.50	1.00	8.70	7.72	215.00	35.90	5.15	6.17	11.40	37.80	0.22	1.31	7.62	0.61	3.95
E19-218	81.10	313.00	1128.00	12.70	4.05	13.70	34.40	1.12	5.18	7.02	416.00	28.50	7.58	7.29	11.80	34.00	0.25	1.80	7.04	0.58	4.90
E19-223	87.10	279.00	1022.00	12.90	4.19	16.30	36.60	1.25	7.27	7.27	43.60	35.50	7.39	6.77	11.30	30.60	0.20	1.62	8.47	0.58	5.03
E19-221	82.50	265.00	929.00	14.10	5.34	17.30	38.00	1.20	7.82	7.41	45.90	38.30	8.48	6.22	10.70	41.40	0.19	1.16	7.17	0.72	5.13
E19-219	88.40	283.00	925.00	12.40	8.54	18.70	106.00	3.09	10.90	9.36	66.60	56.70	11.40	7.22	13.20	63.90	0.17	0.85	6.64	0.91	11.32
Average	82.05	315.10	1020.19	13.37	5.67	12.22	44.48	1.40	9.42	7.70	90.63	41.92	8.83	7.09	11.60	46.67	0.19	1.39	7.79	0.73	5.75
UCC	84.00	320.00	624.00	17.00	10.50	2.70	193.00	5.30	21.00	14.00	97.00	92.00	28.00	17.30	47.00	67.00	0.15	1.65	8.76	0.75	13.79

UCC: Upper continental crust, quoted in Rudnick and Gao.

The trace elements are normalized by the upper continental crust (UCC) (Figure 5). The majority of trace elements (Pb, Sc, Cr, Zn, Th, Zr, Hf, Cu, Co and Ni) are lower in the sandstone than in the UCC, but Ba and U are enriched, and Rb and Sr are comparable. Except for three sandstone samples in which V is greater than that in the UCC, the remainder are lower. The Sc/Cr, Co/Th, Cr/Th, Th/Sc and Zr/Sc ratios are presented in Table 2.

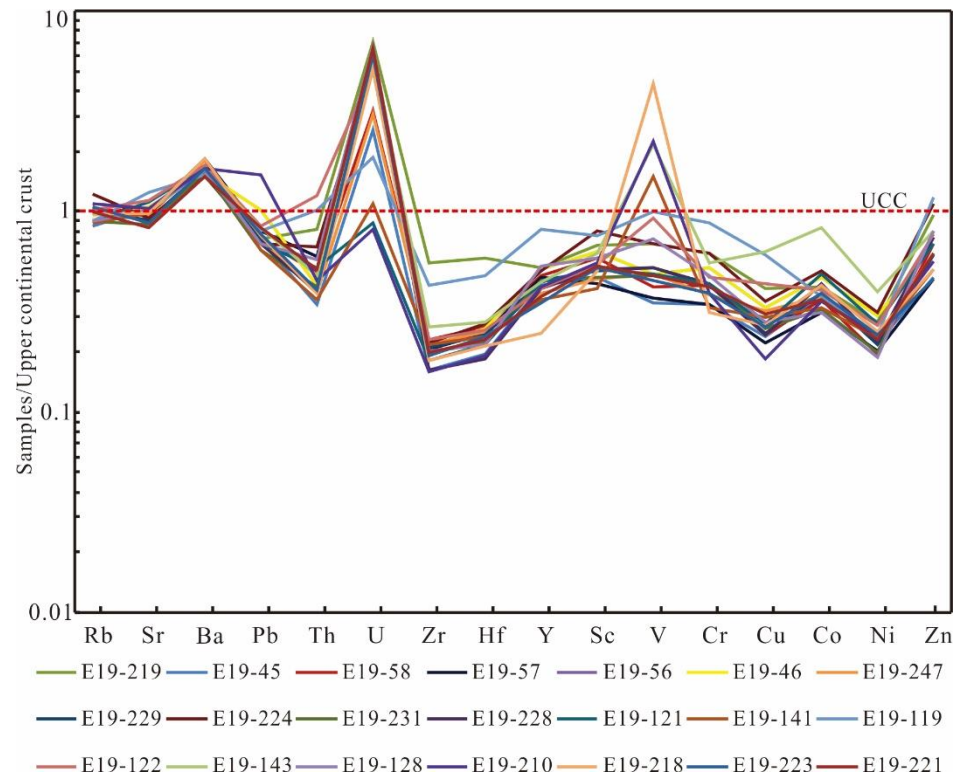


Figure 5. The standardized distribution curve of the upper continental crust of trace elements; UCC: upper continental crust is quoted from Rudnick and Gao [33].

4.4. Rare Earth Element (REE) Geochemistry

The concentrations and ratios of the REEs in the sandstone samples are shown in Table 3. The REE distribution of the Zhiluo Formation sandstone is generally inclined to the right, showing LREE enrichment and HREE loss (Figure 6). The uniform chondrite normalized pattern suggests that these sandstones may have the same provenance, sedimentary environment and tectonic setting. The Eu/Eu^* and Ce/Ce^* ratios of the sandstones are calculated using the following formulas: $\text{Eu}/\text{Eu}^* = 2 \times \text{Eu}_{\text{CN}} / (\text{Sm}_{\text{CN}} + \text{Gd}_{\text{CN}})$ and $\text{Ce}/\text{Ce}^* = 2 \times \text{Ce}_{\text{CN}} / (\text{La}_{\text{CN}} + \text{Pr}_{\text{CN}})$. Table 3 shows the normalized ratios $(\text{La}/\text{Yb})_{\text{CN}}$, $(\text{La}/\text{Sm})_{\text{CN}}$ and $(\text{Gd}/\text{Yb})_{\text{CN}}$.

Table 3. Rare earth element concentrations of sandstones from the Zhiluo Formation.

Sample No.	La	Ce	Pr	Nd	Sm	Eu	Gd	Tb	Dy	Ho	Er	Tm	Yb	Lu	Y	ΣREE	ΣLREE	ΣHREE	ΣLREE/ΣHREE	(La/Yb) _{CN}	(La/Sm) _{CN}	(Gd/Yb) _{CN}	Eu/Eu*	Ce/Ce*
E19-45	21.50	40.10	4.78	17.50	2.85	1.18	2.38	0.37	1.82	0.33	0.96	0.16	1.02	0.14	8.89	103.98	87.91	16.07	5.47	14.24	4.75	1.89	1.35	0.90
E19-58	26.10	48.40	5.69	21.10	3.30	1.15	2.80	0.42	2.03	0.36	1.04	0.17	1.06	0.15	10.00	123.77	105.74	18.03	5.86	16.64	4.98	2.14	1.13	0.90
E19-57	31.40	56.40	6.63	23.70	3.55	1.22	3.02	0.44	2.12	0.37	1.09	0.18	1.13	0.15	9.82	141.22	122.90	18.32	6.71	18.78	5.57	2.17	1.11	0.88
E19-56	26.60	47.50	5.55	20.20	3.21	1.22	2.76	0.41	1.97	0.35	1.04	0.17	1.10	0.15	9.28	121.50	104.28	17.22	6.05	16.34	5.22	2.03	1.22	0.88
E19-46	25.70	47.30	5.59	20.60	3.39	1.17	2.74	0.44	2.16	0.41	1.22	0.21	1.34	0.17	10.80	123.23	103.75	19.48	5.33	12.96	4.77	1.66	1.14	0.89
E19-247	23.40	42.10	5.03	18.90	2.98	1.10	2.47	0.39	1.86	0.33	0.98	0.17	0.99	0.14	8.21	109.05	93.51	15.54	6.02	15.92	4.94	2.02	1.21	0.88
E19-229	28.90	52.10	5.96	21.80	3.53	1.12	2.94	0.44	2.11	0.35	1.12	0.17	1.08	0.14	9.36	131.12	113.41	17.71	6.40	18.08	5.15	2.21	1.03	0.89
E19-224	36.70	66.20	7.66	27.60	4.31	1.11	3.55	0.52	2.39	0.40	1.26	0.19	1.13	0.16	10.60	163.77	143.58	20.19	7.11	21.95	5.36	2.55	0.84	0.89
E19-231	26.20	47.50	5.63	20.90	3.31	1.11	2.82	0.43	2.05	0.35	1.12	0.17	1.05	0.14	9.51	122.30	104.65	17.65	5.93	16.86	4.98	2.18	1.08	0.88
E19-228	23.80	41.60	4.91	18.20	2.96	1.11	2.50	0.38	1.85	0.33	1.01	0.15	0.95	0.13	8.62	108.49	92.58	15.91	5.82	16.98	5.06	2.14	1.22	0.86
E19-121	26.50	45.00	5.57	20.20	3.17	1.24	2.70	0.40	1.98	0.35	1.07	0.17	1.10	0.16	9.27	118.89	101.68	17.21	5.91	16.28	5.26	1.99	1.26	0.83
E19-141	22.50	40.30	4.84	17.80	2.83	1.23	2.33	0.35	1.67	0.30	0.88	0.14	0.92	0.13	7.58	103.80	89.50	14.30	6.26	16.62	5.00	2.06	1.42	0.87
E19-119	42.10	90.20	9.31	34.10	5.39	1.40	4.56	0.69	3.30	0.61	1.78	0.30	1.91	0.27	16.90	212.82	182.50	30.32	6.02	14.89	4.92	1.93	0.84	1.03
E19-122	33.70	59.50	6.41	23.00	3.40	1.19	2.86	0.40	1.88	0.33	1.01	0.16	1.02	0.14	8.61	143.62	127.20	16.42	7.75	22.33	6.24	2.27	1.14	0.90
E19-143	27.00	47.50	5.54	20.90	3.33	1.24	2.74	0.41	2.08	0.38	1.10	0.19	1.26	0.19	9.32	123.18	105.51	17.67	5.97	14.48	5.10	1.76	1.22	0.87
E19-128	29.00	52.00	6.00	22.20	3.43	1.23	2.85	0.44	2.21	0.41	1.20	0.20	1.32	0.19	11.20	133.88	113.86	20.02	5.69	14.85	5.32	1.75	1.17	0.88
E19-210	27.10	44.80	5.29	19.80	3.11	1.11	2.67	0.39	1.84	0.32	0.99	0.15	0.94	0.13	8.70	117.34	101.21	16.13	6.27	19.59	5.48	2.31	1.15	0.83
E19-218	20.30	37.50	4.46	16.60	2.64	0.92	2.00	0.30	1.31	0.21	0.68	0.11	0.70	0.09	5.18	93.00	82.42	10.58	7.79	19.74	4.84	2.33	1.17	0.89
E19-223	23.80	43.30	5.19	18.90	3.05	1.05	2.57	0.38	1.68	0.29	0.88	0.13	0.81	0.12	7.27	109.42	95.29	14.13	6.75	19.81	4.91	2.57	1.12	0.88
E19-221	26.70	47.10	5.57	20.80	3.42	0.98	2.77	0.40	1.84	0.30	0.95	0.13	0.84	0.12	7.82	119.74	104.57	15.17	6.89	21.38	4.91	2.66	0.95	0.87
E19-219	37.70	68.00	7.93	28.50	4.40	1.08	3.53	0.55	2.54	0.43	1.40	0.23	1.51	0.21	10.90	168.90	147.61	21.29	6.93	16.87	5.39	1.89	0.81	0.88
Average	27.94	50.69	5.88	21.59	3.41	1.15	2.84	0.43	2.03	0.36	1.08	0.17	1.10	0.15	9.42	128.24	110.65	17.59	6.33	17.41	5.15	2.12	1.12	0.89
UCC	31.00	63.00	7.10	27.00	4.70	1.00	4.00	0.70	3.90	0.83	2.30	0.30	1.96	0.31	21.00	148.10	133.80	14.30	9.30	10.50	4.20	1.60	0.72	–

UCC: Upper continental crust, quoted in Rudnick and Gao. LREE = La + Ce + Pr + Nd + Sm + Eu; HREE = Gd + Tb + Dy + Ho + Er + Tm + Yb + Lu.

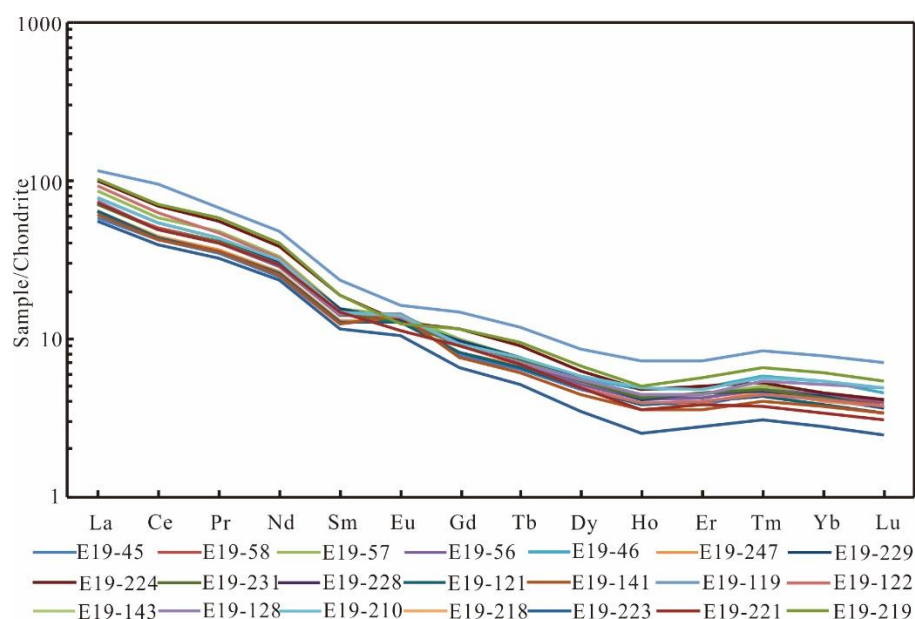


Figure 6. Chondrite-normalized REE diagram for the Zhiluo Formation sandstones. Standardized chondrite data is quoted from Taylor and McLennan [34].

The total amount of rare earth elements (Σ REE) ranges from 93 ppm to 212.82 ppm (average 128.24 ppm), the LREE contents vary between 82.42 ppm and 182.5 ppm (average 110.65 ppm), and the HREE contents vary between 10.58 ppm and 30.32 ppm (average 17.59 ppm). The LREE/HREE ratios vary from 5.33 to 7.79 (average 6.33). The Eu/Eu* ratio shows positive anomalies and varies from 0.81 to 1.42 (average 1.12). The Ce/Ce* ratio varies from 0.83 to 1.03 (average 0.89). The ratio of (La/Yb)_{CN} is between 12.96 and 22.33, with an average of 17.41, which fully illustrates the obvious fractionation between the LREEs and HREEs. The (La/Sm)_{CN} results indicated that the LREE fractionation ratio is between 4.75 and 6.24, with an average of 5.15; however, the (Gd/Yb)_{CN} ratio, which reflects the fractionation ratio of HREE, is between 1.66 and 2.66, with an average of 2.12.

5. Discussion

5.1. Provenance

5.1.1. Provenance from Petrography

The Zhiluo Formation sandstone is rich in quartz and feldspar, indicating that it is not derived from basic rock and that its source area hosted feldspar source rock. Some quartz particles exhibit secondary enlargement edge phenomena, which are caused by the recycling of sedimentary quartz throughout diagenesis. Chloritization can be seen in some plagioclases. There are many types of debris, mainly igneous rock debris, metamorphic rock debris and sedimentary rock debris, in this rock, indicating corresponding provenance of the deep igneous rocks, ancient sediments and metamorphic rock in the northern part of the basin. The heavy minerals include a small amount of epidote, indicating that they are mainly derived from metamorphic rocks; in addition, zircon, biotite and tourmaline heavy mineral assemblages show that the parent rocks may have been moderately acidic magmatic rocks and metamorphic rocks [35]. In summary, the parent rock of the Zhiluo Formation sandstone is feldspathic sandstone from an intermediate-acidic source area.

5.1.2. Provenance and Source Rock from Geochemistry

The provenance and source rocks of clastic sedimentary rocks can be identified by using different discrimination diagrams of major elements and trace elements [2,36,37]. Proposed by Roser and Korsch, the DF1–DF2 discrimination diagram [38] (Figure 7) is based on the content of major elements in 248 groups of sandstone and mudstone, which effectively

divides the source area into mafic igneous provenance, intermediate igneous provenance, felsic igneous provenance and quartzose sedimentary provenance. The majority of the studied sandstone samples plot in the quartzose sedimentary provenance, and one sample falls within the felsic igneous provenance.

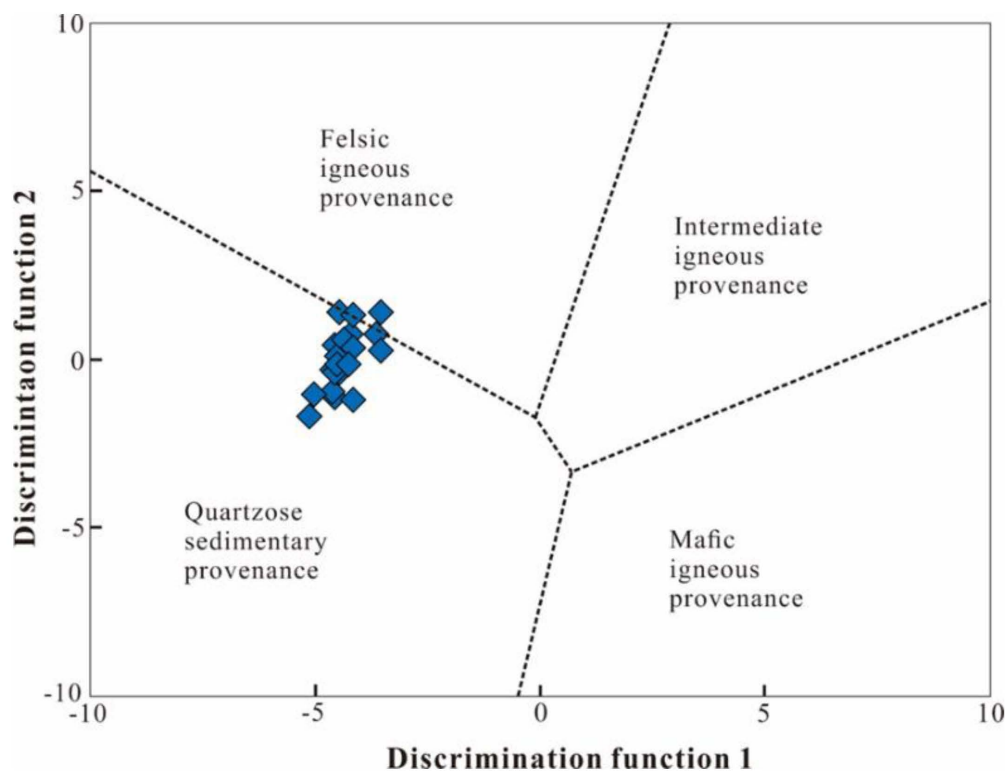


Figure 7. Provenance discriminant function using major elements [38]. 13. $DF1 = -1.772TiO_2 + 0.607Al_2O_3 + 0.76Fe_2O_3^T - 1.5MgO + 0.616CaO + 0.509Na_2O - 1.224K_2O - 9.09$; $DF2 = 0.445TiO_2 + 0.07Al_2O_3 - 0.25Fe_2O_3^T - 1.142MgO + 0.438CaO + 1.475Na_2O + 1.426K_2O - 6.861$.

At the same time, because Al, Ti and Zr oxides and hydroxides have low solubility in low-temperature aqueous solutions, they may be termed immobile elements; thus, the Al_2O_3/TiO_2 ratio of the samples is very close to that of their source rocks. For the intermediate igneous provenance, this ratio is between 8 and 21; when the provenance is felsic, the ratio is more than 21; the ratio < 8 indicates basic source rock [38]. The Al_2O_3/TiO_2 ratio of the sandstone samples varies from 15.45 to 42.83, with an average of 28.75. The majority of sandstone samples are in the range of felsic rock, and only a few samples plot in the range of intermediate igneous rock. In addition, the Al_2O_3 versus TiO_2 diagram [29] (Figure 8) illustrates that most samples fall in the felsic rock field, and only two samples plot in the range of intermediate igneous rock area.

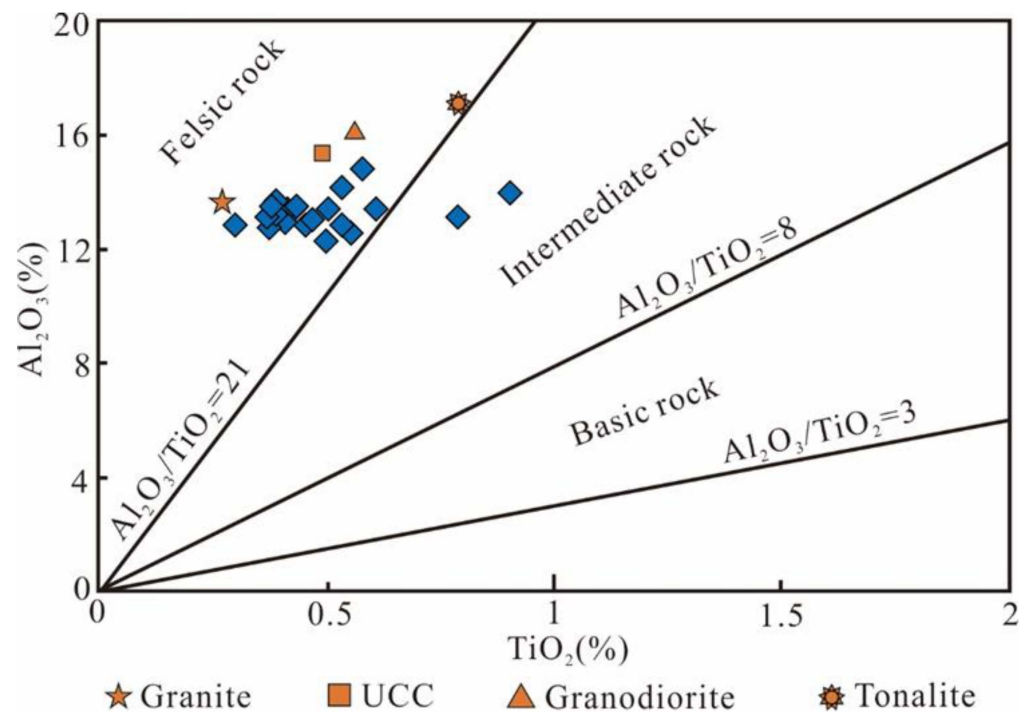


Figure 8. The plot of Al_2O_3 versus TiO_2 [19] of the Zhiluo Formation sandstones: UCC [39], granite [40], granodiorite [41] and tonalite [41].

The K_2O versus Rb diagram and TiO_2 versus Ni diagram (Figure 9) can be used to distinguish the composition of the source area [42,43]. In the K_2O versus Rb diagram (Figure 9a), all samples in the study area plot within the area with the field of intermediate to felsic rock, and in the TiO_2 versus Ni diagram (Figure 9b), the sandstone samples are mainly concentrated in the acidic rock area. The two diagrams show that the source rocks of the Zhiluo sandstone are felsic to intermediate igneous source rocks.

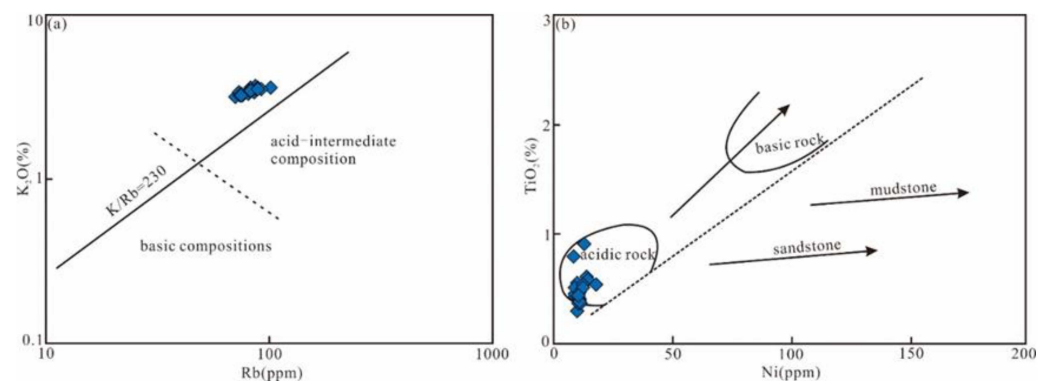


Figure 9. Source material composition discrimination diagrams for the Zhiluo Formation sandstones. (a) K_2O versus Rb bivariate diagram [42]; (b) TiO_2 versus Ni bivariate diagram [43].

Trace elements such as Ti, Hf, Sc, Th, Zr, Y and REEs are critical for interpreting the origin and composition of the source area due to their minimal possibility of migrating during the post-depositional process [44]. Hf versus La/Th [42], La/Sc versus Co/Th [10], Cr/Th versus Th/Sc [45] and Y/Ni versus Cr/V [10] discrimination diagrams (Figure 10) were used to analyze the parent rock types of sandstones. The studied sandstones, according to these diagrams, are the felsic igneous source rocks and intermediate igneous rocks.

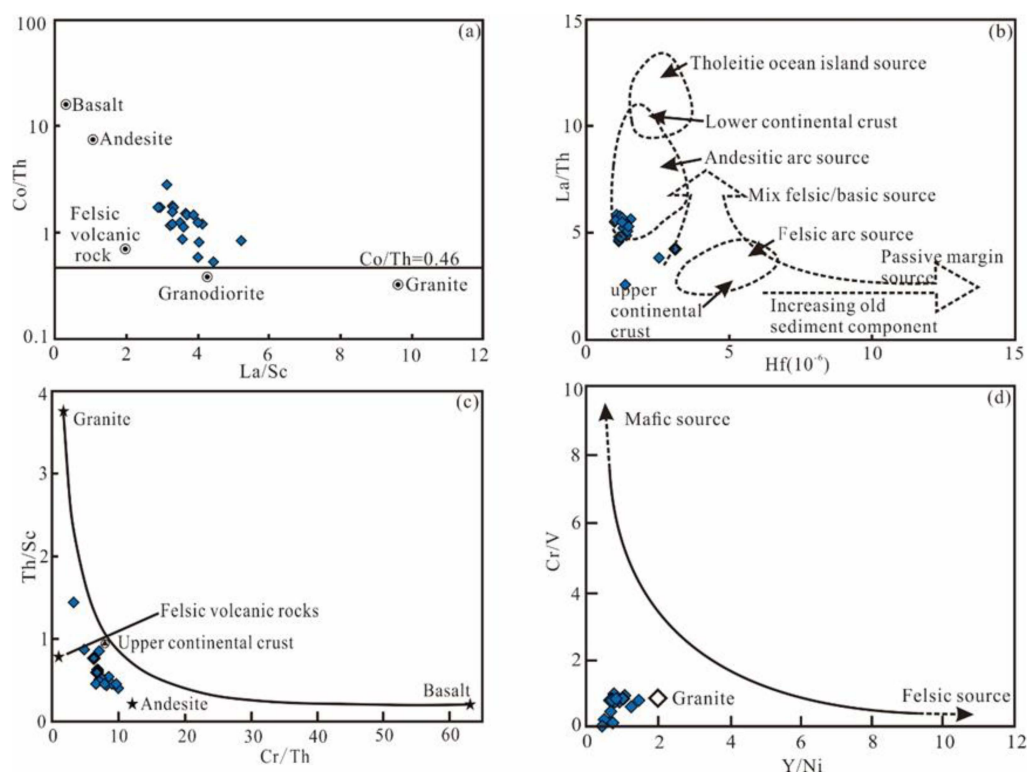


Figure 10. Source rock discrimination diagram for the Zhiluo Formation sandstones. (a) La/Sc versus Co/Th bivariate diagram [10], (b) Hf (ppm) versus La/Th bivariate diagram [42], (c) Cr/Th versus Th/Sc bivariate diagram [45] and (d) Y/Ni versus Cr/V bivariate diagram [10].

Plotting on the Ni-V-Th*10 ternary diagram [46] (Figure 11) shows that the Zhiluo Formation sandstones fall near the V-Th*10 line, reflecting that the provenance of sandstone samples are felsic igneous rocks.

Comparing the Eu/Eu*, Cr/Th, Th/Co, Th/Sc, La/Co, Th/Sc and La/Sc ratios of the Zhiluo Formation sandstones with the UCC and the range of sediments from felsic sources and mafic sources [2,47,48] (Table 4) shows that the sandstones are derived from felsic rocks.

Table 4. Comparison of characteristic parameters of trace elements in sandstones between the Zhiluo Formation and different source areas.

Elemental Ratio	Sandstone Samples		Range of Sediments from Felsic Source [2,49]	Range of Sediments from Mafic Source [50]	UCC [33]
	Range	Average			
Eu/Eu*	0.81~1.42	1.12	0.40–0.94	0.71–0.95	0.72
La/Sc	2.89~5.21	3.65	2.50–16.3	0.43–0.86	2.21
La/Co	1.89~6.57	4.11	1.80–13.8	0.14–0.38	1.79
Th/Sc	0.52~1.64	0.73	0.84–20.05	0.05–0.22	0.75
Th/Co	0.35~1.80	0.83	0.67–19.4	0.04–1.40	0.61
Cr/Th	3.45~10.69	7.79	4–15	25–500	8.96

Previous studies [25] on zircon ages show that the Zhiluo Formation sandstone in the Bayinqinggeli region are mainly concentrated in Paleozoic. Due to the influence of the activity of the Yinshan orogenic belt in the north, multiple volcanic eruptions and large-scale intermediate-acid magmatic intrusions occurred, and a large area of Paleozoic compound intermediate-acid intrusive rocks developed. Combining this information with the discrimination diagrams of the major elements, trace elements and rare earth elements in the sandstone of the Zhiluo Formation, it is speculated that the parent rock of the

Zhiluo Formation sandstone is the intermediate-acid magmatic rock developed during the Paleozoic in the Yinshan orogenic belt in the northern basin.

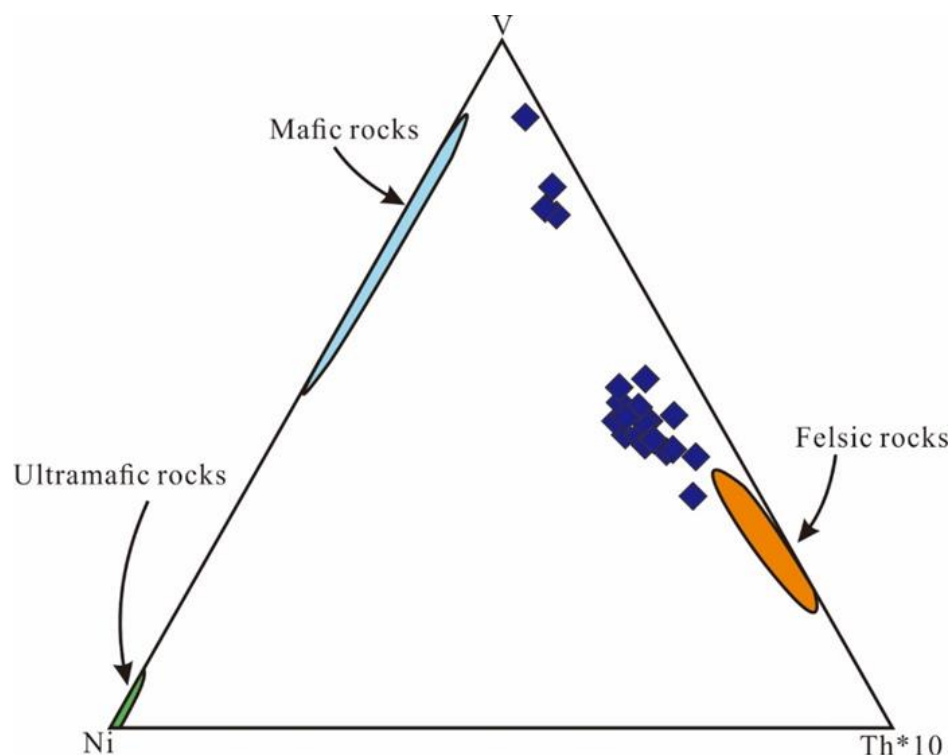


Figure 11. Ni-V-Th*10 ternary diagram for provenance discrimination of the Zhiluo Formation sandstones [46].

5.2. Tectonic Setting

The geochemical characteristics of siliciclastic sediments can reflect not only the characteristics of the source area and the geochemical features of the parent rock but also the tectonic settings of sedimentary basins. Sedimentary rocks from different tectonic settings have obvious differences in the composition and content of elements [44,51].

The discrimination diagrams based on major elements were proposed by Maynard, Roser and Korsch, and they are usually used in sandstones to discriminate source rocks. The SiO_2 versus $\text{K}_2\text{O}/\text{Na}_2\text{O}$ [36] and $\text{K}_2\text{O}/\text{Na}_2\text{O}$ versus $\text{SiO}_2/\text{Al}_2\text{O}_3$ [52] diagrams (Figure 12a,b) show that all sandstone samples of the Zhiluo Formation fall within the passive margin field. Furthermore, Bhatia [53] found that SiO_2 , $\text{K}_2\text{O}/\text{Na}_2\text{O}$, $\text{SiO}_2/\text{Al}_2\text{O}_3$, $\text{Al}_2\text{O}_3/(\text{CaO} + \text{Na}_2\text{O})$ and $\text{Fe}_2\text{O}_3^{\text{T}} + \text{MgO}$ are the most representative parameters in source tectonic setting discrimination; thus, he proposed the $\text{Fe}_2\text{O}_3^{\text{T}} + \text{MgO}$ versus $\text{Al}_2\text{O}_3/(\text{CaO} + \text{Na}_2\text{O})$ diagram [53] (Figure 12c), which shows that the majority of the sandstone samples are distributed within the passive margin field, with some samples nearby. In addition, according to the comparison of characteristic parameters between the sandstones of the Zhiluo Formation and sandstones in four different tectonic settings (Table 5), the major elements characteristics of sandstones of the Zhiluo Formation are most consistent with the passive margin setting.

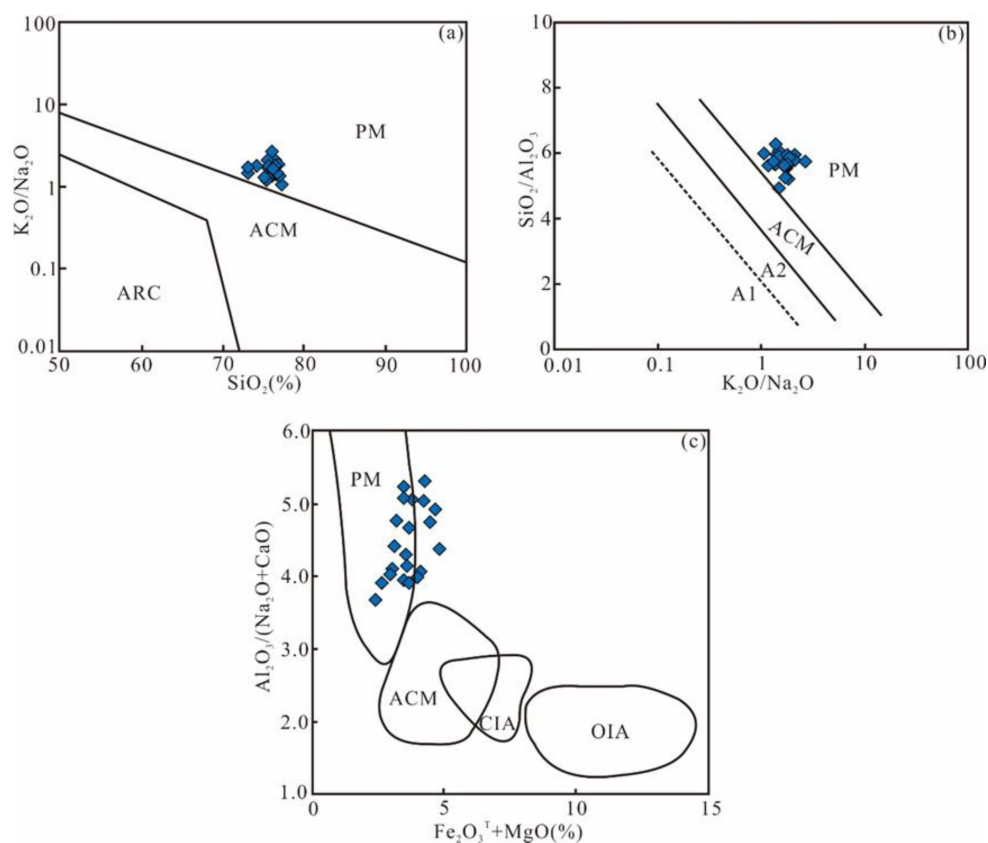


Figure 12. Plots of major element composition of the Zhiluo Formation sandstones using tectonic discrimination diagrams: (a) SiO₂ versus K₂O/Na₂O bivariate diagram [36], (b) K₂O/Na₂O versus SiO₂/Al₂O₃ bivariate diagram [52] and (c) Fe₂O₃^T + MgO versus Al₂O₃/(Na₂O + CaO) bivariate diagram [53]. PM = passive margin; ACM = active continental margin; ARC, A1 and A2 = arc; CIA = continental island arc; OIA = ocean island arc.

Table 5. Comparison of characteristic parameters of major elements of sandstones between the Zhiluo Formation and other tectonic settings.

Tectonic Setting	Major Element Characteristic Parameters				
	Fe ₂ O ₃ ^T + MgO	TiO ₂	Al ₂ O ₃ /SiO ₂	K ₂ O/Na ₂ O	Al ₂ O ₃ /(CaO + Na ₂ O)
Ocean Island Arc	11.73	1.06	0.29	0.39	1.72
Continental Island Arc	6.79	0.64	0.20	0.61	2.42
Active Continental Margin	4.63	0.46	0.18	0.99	2.56
Passive Margin	2.89	0.49	0.10	1.60	4.15
Sandstone of the Zhiluo Formation	3.64	0.49	0.17	1.64	4.15

Traditional diagrams have been called into doubt in recent years because they cannot explain the distinction between continental island arcs (CIAs) and active continental margins (ACMs), nor can they distinguish among the arc, collision and continental rift. To determine the tectonic setting, numerous diagrams must be combined. In 2013, Verma and Armstrong-Altrin [47] proposed a new discriminant diagram for tectonic setting based on the discriminant function, which can distinguish continental rift, island arc and continental collision. In the DF2(Arc-Rift-Col)_{m1} versus DF1(Arc-Rift-Col)_{m1} discrimination diagram [47] (Figure 13), except for one sample that plots in the collision field, the sandstone samples of the Zhiluo Formation mostly plot within the continental rift area. Based on these discriminant diagrams, Verma and Armstrong-Altrin [41] proposed a new discriminant diagram, which uses isometric log-ratio transformation during data processing to eliminate

the close effect of data. The diagrams [41] (Figure 14) obtained by isometric log-ratio (ilr) transformation of all the major elements and some trace elements reflect a passive margin background for the source area. This is consistent with the traditional graphical results for the Zhiluo Formation.

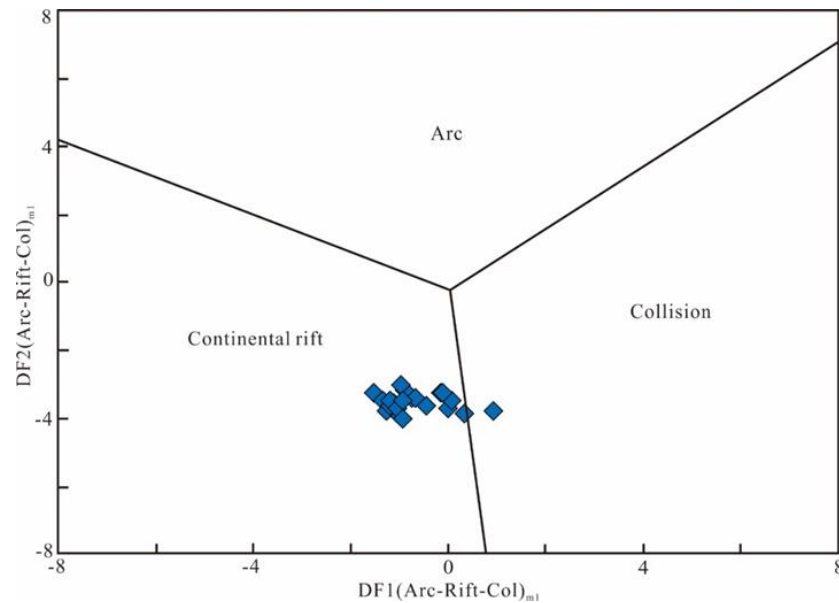


Figure 13. Tectonic setting discrimination of Zhiluo Formation [47]. $DF1(Arc-Rift-Col)_{m1} = (-0.263) \times \ln(TiO_2/SiO_2)_{adj} + 0.604 \times \ln(Al_2O_3/SiO_2)_{adj} + (-1.725) \times \ln(Fe_2O_3^T/SiO_2)_{adj} + 0.660 \times \ln(MnO/SiO_2)_{adj} + 2.191 \times \ln(MgO/SiO_2)_{adj} + 0.144 \times \ln(CaO/SiO_2)_{adj} + (-1.304) \times \ln(Na_2O/SiO_2)_{adj} + 0.054 \times \ln(K_2O/SiO_2)_{adj} + (-0.330) \times \ln(P_2O_5/SiO_2)_{adj} + 1.588$; $DF2(Arc-Rift-Col)_{m1} = (-1.196) \times \ln(TiO_2/SiO_2)_{adj} + 1.064 \times \ln(Al_2O_3/SiO_2)_{adj} + 0.303 \times \ln(Fe_2O_3^T/SiO_2)_{adj} + 0.436 \times \ln(MnO/SiO_2)_{adj} + 0.838 \times \ln(MgO/SiO_2)_{adj} + (-0.407) \times \ln(CaO/SiO_2)_{adj} + 1.021 \times \ln(Na_2O/SiO_2)_{adj} + (-1.706) \times \ln(K_2O/SiO_2)_{adj} + (-0.126) \times \ln(P_2O_5/SiO_2)_{adj} - 1.068$.

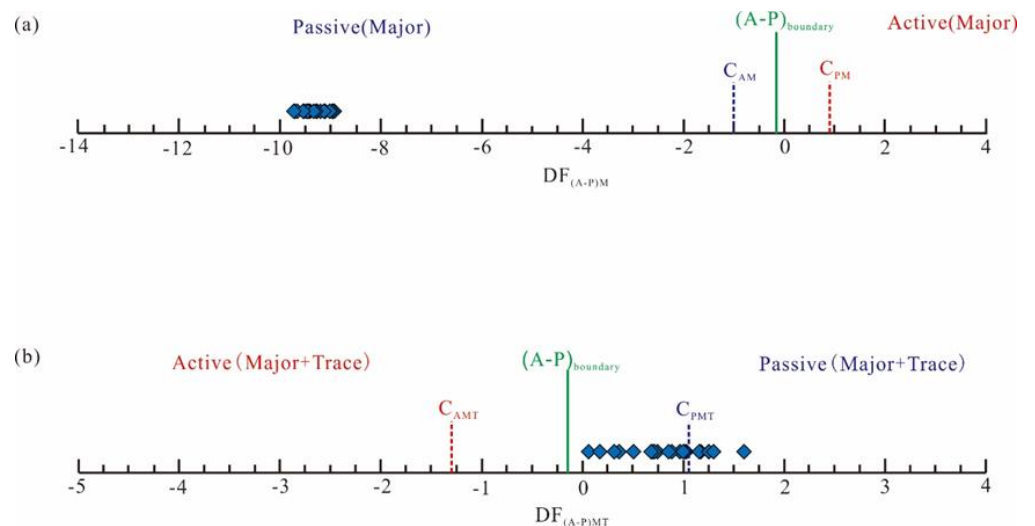


Figure 14. Tectonic setting discrimination of the Zhiluo Formation sandstones [41]. (a) ilr based on major elements; (b) ilr based on major elements and some trace elements. $DF_{(A-P)M} = (3.0005 \times ilr1TiM) + (2.8243 \times ilr2AlM) + (-1.596 \times ilr3FeM) + (-0.7056 \times ilr4MnM) + (-0.3044 \times ilr5MgM)$

$$\begin{aligned}
& + (0.6277 \times \text{ilr6CaM}) + (-1.1838 \times \text{ilr7NaM}) + (1.5915 \times \text{ilr8KM}) + (0.1526 \times \text{ilr9PM}) - 5.9948; \\
\text{DF}_{(\text{A-P})\text{MT}} & = (3.2683 \times \text{ilr1TiMT}) + (5.3873 \times \text{ilr2AlMT}) + (1.5546 \times \text{ilr3FeMT}) + (3.2166 \times \text{ilr4MnMT}) \\
& + (4.7542 \times \text{ilr5MgMT}) + (2.0390 \times \text{ilr6CaMT}) + (4.0490 \times \text{ilr7NaMT}) + (3.1505 \times \text{ilr8KMT}) + (2.3688 \\
& \times \text{ilr9PMT}) + (2.8354 \times \text{ilr10CrMT}) + (0.9011 \times \text{ilr11NbMT}) + (1.9128 \times \text{ilr12NiMT}) + (2.9094 \times \\
& \text{ilr13VMT}) + (4.1507 \times \text{ilr14YMT}) + (3.4871 \times \text{ilr15ZrMT}) - 3.208.
\end{aligned}$$

5.3. Source Area Paleoweathering and Paleoclimate

5.3.1. Paleoweathering

The kinds and properties of the parent rocks in the source area have a considerable influence on the composition of the sandstones, but they are still affected by a series of processes such as weathering, transportation and deposition [44]. Therefore, the chemical composition of sandstone can reflect the progress of weathering in parent rock areas [54]. In general, chemical weathering has a substantial influence on the major and trace element compositions of siliciclastic deposits in humid climates. Some larger cations, such as Al, Rb and Ba, can migrate more selectively than smaller cations (such as Na, Sr and Ca). These geochemical characteristics can eventually be transferred to sediments, which provides important information for monitoring the weathering status of the sediment source area [55]. Thus, geochemical proxies are significant indicators of the source area.

The weathering products of parent rock are the main material sources of sedimentary rocks. Chemical weathering and diagenesis in the upper crust have the greatest impact on feldspar, resulting in the formation of clay minerals. The A-CN-K (Al_2O_3 - CaO^* + Na_2O - K_2O) ternary diagram [30], where Al_2O_3 , CaO^* , Na_2O and K_2O are in molecular proportions, can not only directly reflect the trend and degree of weathering of sediments, but also indicate the compositional characteristics of source rocks. The CIA is an essential indicator for determining the degree of weathering in the provenance area, and it is commonly plotted in the A-CN-K ternary diagram to determine the source rock composition. Here, the chemical indices of PIA and ICV are also employed to assess the source region paleoweathering.

By calculating the CIA values, the weathering degree of the source area can be distinguished, which is usually divided into the following three cases: (a) $\text{CIA} > 80$: implies strong chemical weathering of the source area; (b) $\text{CIA} = 60\text{--}80$: indicates moderate chemical weathering of the source area; and (c) $\text{CIA} < 60$, represents initial chemical weathering of the source area [30]. The CIA values of the studied sandstones vary from 56.30 to 63.04 (average 59.75) (Table 1), which is less than 60 and corresponds to case c. These values indicate that the sediments formed from source rocks that had not undergone chemical degradation. This is also evident from the A-CN-K ternary plot [30] (Figure 15), where predominantly the samples plot near the connection line between plagioclase and clay minerals, parallel to the A-CN side, which shows that the chemical weathering in the provenance area corresponds to the initial chemical weathering.

The ICV is used to determine the degree of change in the original components of clastic rocks. Generally, it is divided into the following two situations: if the ICV is greater than 1, it indicates that the clastic rock is the sediment of the first deposition; if the ICV value is less than 1, it indicates that the clastic rocks are recycled sediments or sediments had undergone strong weathering [29]. The ICV values of the studied samples are 0.74–0.91 (average 0.82), all less than 1; thus, these values indicate that the Zhiluo Formation sandstones are recycled sediments.

Sedimentary sorting and recycling usually cause selective enrichment of elements. Th and Sc are difficult to dissolve in formation water, so the Th/Sc ratio does not change in the process of sedimentary recycling. The Th/Sc and Zr/Sc ratios show good positive correlations, revealing that the provenance had a compositional change similar to magmatic differentiation [10]. In the Th/Sc versus Zr/Sc diagram [10] (Figure 16), all the sandstone samples fall near the UCC and do not show a positive correlation, indicating that the clastic rock components had experienced recycling, which is consistent with the ICV results.

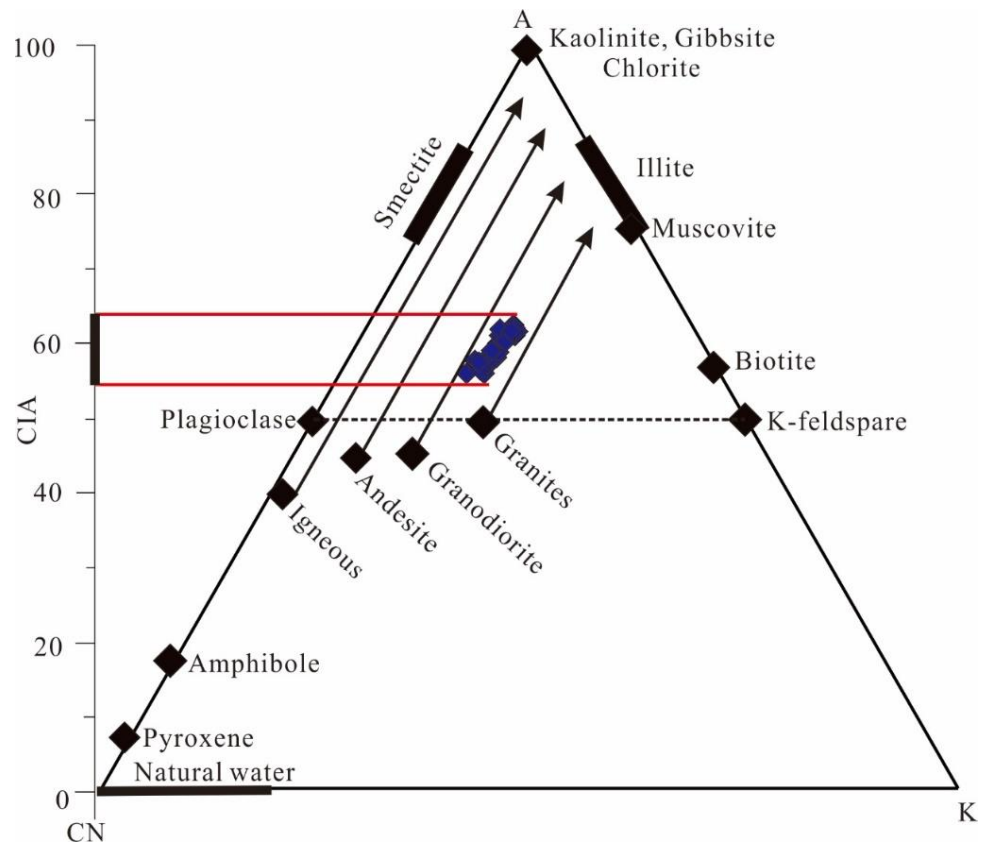


Figure 15. A-CN-K Ternary diagram for the Zhiluo Formation sandstones [30]: A = Al_2O_3 ; CN = $CaO^* + Na_2O$; and K = K_2O .

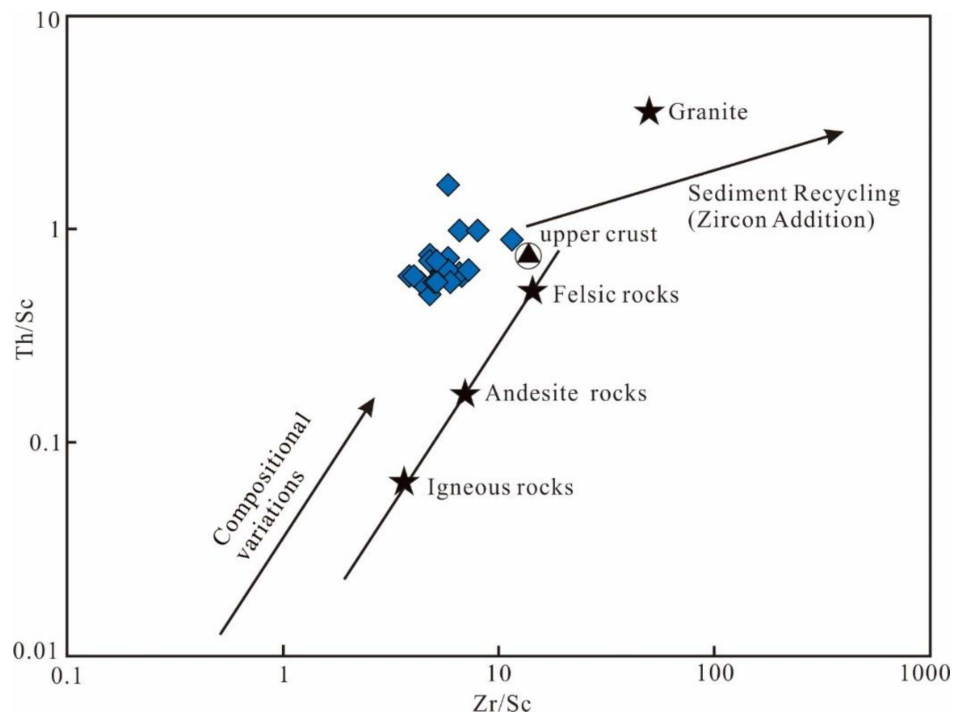


Figure 16. Th/Sc versus Zr/Sc bivariate diagram [10] showing the influence of weathering, sorting and recycling processes for sandstones from the Zhiluo Formation.

In 1995, Fedo proposed a new index of plagioclase alteration (PIA), which eliminates the effect of K_2O in the calculation and can better determine the weathering of the parent rock and source area [30]. The PIA of the Zhiluo Formation sandstones ranges from 57.51 to 71.65 (average 67.38), indicating that there was moderately weak weathering in the source area. In general, with increasing of sediment transport distance, weathering and denudation will be stronger. It can be inferred that the Zhiluo Formation sandstones may have been subject to medium to short distance transportation, corresponding to near-source deposition.

5.3.2. Paleoclimate

Geochemical proxies have frequently been employed to interpret the paleoclimate of the source area. The parent rocks and clastic sediments in the provenance area are affected by climatic conditions [11,29,56]. Chemical weathering mainly occurs under humid climates, which results in the removal of mobile elements (Na, K and Ca) and the concentrations of immobile elements (Al and Si). Therefore, the paleoclimate can be deduced by the geochemical characteristics of the sandstone [11].

The $SiO_2\%$ versus $Al_2O_3 + K_2O + Na_2O\%$ bivariate diagram [30] (Figure 17) proposed by Sutter and Dutta in 1986 was applied to determine the relationship between the maturity of sandstone and climate. In this diagram, all the sandstone samples of the Zhiluo Formation fall within the semi-arid climate field, indicating that the sedimentary environment of the Zhiluo Formation has semi-arid climate conditions. The sandstones have experienced mild to moderate weathering under dry paleoclimate conditions, according to the geochemical indicators of the major elements in the siliceous clastic deposits (CIA, PIA, and ICV) (Table 1). This is reasonably consistent with the results of earlier studies in the area.

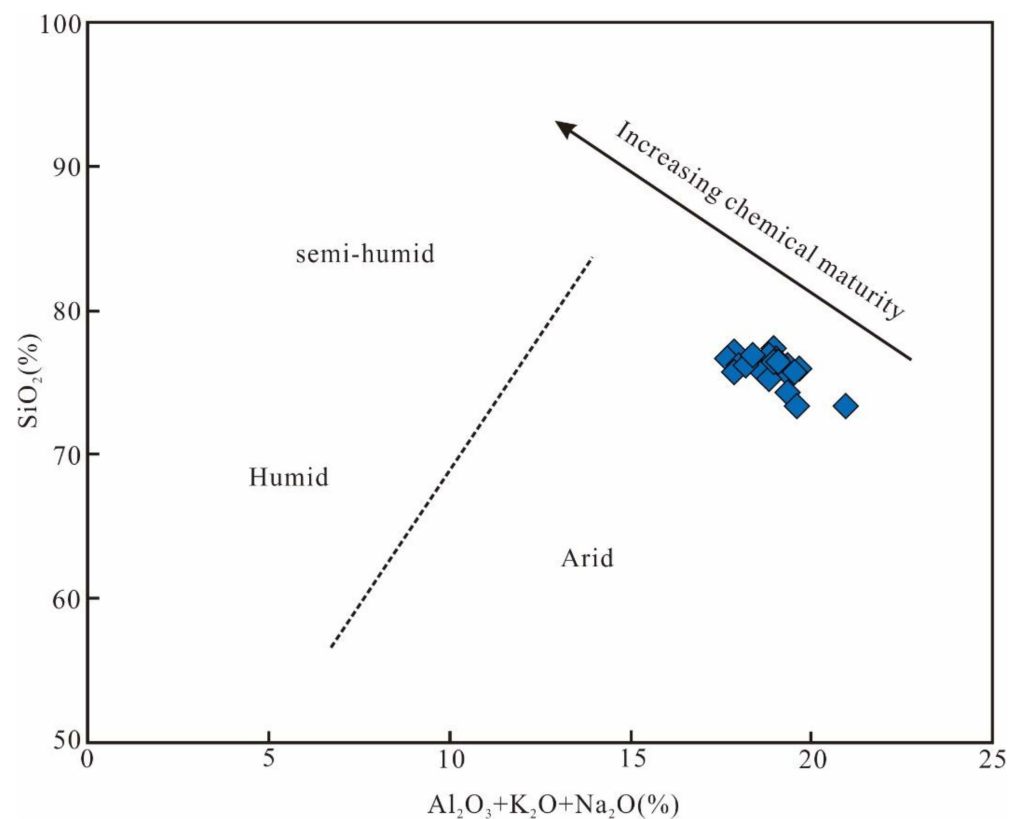


Figure 17. $SiO_2\%$ versus $Al_2O_3 + K_2O + Na_2O\%$ bivariate diagram for distinguishing climatic conditions of the Zhiluo Formation sandstones [30].

6. Conclusions

Based on the petrographic and geochemical characteristics of the Zhiluo Formation sandstones of the Bayinlinggeli sandstone-type uranium deposit in the northern Ordos Basin, the provenance, source area properties and tectonic background are analyzed. The sandstones of the Zhiluo Formation are mainly feldspar sandstone, with the highest SiO₂ content, followed by Al₂O₃ and K₂O. The microscopic observations show that the minerals in the sandstones are mostly quartz, feldspar and mica. The consistency of the chondrite normalized REE distribution curve indicates that the Zhiluo Formation sandstone has the same provenance. CIA and ICV values reflect that the sandstones have undergone weak chemical weathering in arid climate conditions. In addition, the A-CN-K ternary diagram, Th/Sc versus Zr/Sc diagram, Cr/Th versus Th/Sc diagram and Cr/V versus Y/Ni diagram show that the source area was ancient sedimentary rocks and moderately acidic rocks (granite, andesite and granodiorite). On the other hand, the characteristics of the major elements, trace elements and rare earth elements show that the tectonic setting of the provenance area was a passive continental margin. The Zhiluo Formation sandstone was derived from the volcanic-sedimentary rock series developed in the northern part of the basin, and the tectonic setting position of the provenance area corresponds to the Yanshan intracontinental orogenic belt on the northern margin of the North China Craton.

Author Contributions: Conceptualization, Y.C. and F.O.; methodology, X.L. (Xiaoneng Luo); software, X.L. (Xianrong Luo) and M.W.; validation, F.O. and Z.Z.; formal analysis, Z.Z.; investigation, Y.C. and R.T.; resources, Z.Z. and X.L. (Xiaoneng Luo); data curation, Y.C.; writing—original draft preparation, Y.C. and F.O.; writing—review and editing, Y.C. and F.O.; visualization, Y.C. and X.L. (Xiaoneng Luo); supervision, X.L. (Xianrong Luo) and M.W.; project administration, F.O. and Z.Z.; funding acquisition, Z.Z. All authors have read and agreed to the published version of the manuscript.

Funding: This research was financially supported by Uranium Geological Project from the China Nuclear Geological Bureau “Comprehensive Mapping and Selection of Sandstone Type Uranium Deposits in Ganmeng Area” (NO.2021118) and National key research and develop plan projects (NO.2017YFC0602600).

Institutional Review Board Statement: Not applicable.

Informed Consent Statement: Not applicable.

Data Availability Statement: No new data were created in this study. Data sharing is not applicable to this article.

Acknowledgments: We greatly appreciate the help of Yuqi Cai and Panfeng Liu during daily discussion work.

Conflicts of Interest: The authors declare no conflict of interest.

References

1. Suttner, L.J.; Dutta, P.K. Alluvial sandstone composition and paleoclimate, I, Framework mineralogy. *J. Sediment. Petrol.* **1986**, *56*, 329–345.
2. Cullers, R.L. The geochemistry of shales, siltstones and sandstones of Pennsylvanian-Permian age, Colorado, USA: Implications for provenance and metamorphic studies. *Lithos* **2000**, *51*, 181–203. [[CrossRef](#)]
3. Khan, T.; Sarma, D.S.; Somasekhar, V.; Ramanaiah, S.; Reddy, N.R. Geochemistry of the Palaeoproterozoic quartzites of Lower Cuddapah Supergroup, South India: Implications for the palaeoweathering, provenance, and crustal evolution. *Geol. J.* **2020**, *55*, 1587–1611. [[CrossRef](#)]
4. Min-Na, A.; Zhang, F.Q.; Yang, S.F.; Chen, H.L.; Batt, G.E.; Sun, M.D.; Meng, Q.A.; Zhu, D.F.; Cao, R.C.; Li, J.S. Early Cretaceous provenance change in the southern Hailar Basin, northeastern China and its implication for basin evolution. *Cretac. Res.* **2013**, *40*, 21–42. [[CrossRef](#)]
5. Adeigbe, O.C.; Jimoh, Y.A. Geochemical Fingerprints; Implication for Provenance, Tectonic and Depositional Settings of Lower Benue Trough Sequence, Southeastern Nigeria. *J. Environ. Earth Sci.* **2013**, *3*, 115–141.
6. Gao, Y.; Wang, C.; Liu, Z.; Zhao, B.; Zhang, X. Clay mineralogy of the middle Mingshui Formation (upper Campanian to lower Maastrichtian) from the SKIn borehole in the Songliao Basin, NE China: Implications for palaeoclimate and provenance. *Palaeogeogr. Palaeoclimatol. Palaeoecol.* **2013**, *385*, 162–170. [[CrossRef](#)]

7. Salgado-Campos, V.M.J.; Carvalho, I.D.S.; Bertolino, L.C.; Duarte, T.A.; Araújo, B.C.; Borghi, L. Clay mineralogy and litho-geochemistry of lutites from the Lower Cretaceous Crato Member, Araripe Basin, NE Brazil: Implications for paleoenvironmental, paleoclimatic and provenance reconstructions. *J. S. Am. Earth Sci.* **2021**, *110*, 103329. [[CrossRef](#)]
8. Garzanti, E. Petrographic classification of sand and sandstone. *Earth-Sci. Rev.* **2019**, *192*, 545–563. [[CrossRef](#)]
9. Marsaglia, K.M.; Barone, M.; Critelli, S.; Busby, C.; Fackler-Adams, B. Petrography of volcanoclastic rocks in intra-arc volcano-bounded to fault-bounded basins of the Rosario segment of the Lower Cretaceous Alisitos oceanic arc, Baja California, Mexico. *Sediment. Geol.* **2016**, *336*, 138–146. [[CrossRef](#)]
10. McLennan, S.M.; Hemming, S.; McDaniel, D.K.; Hanson, G.N. Geochemical approaches to sedimentation, provenance and tectonics: Processes Controlling the Composition of Clastic Sediments. *Spec. Pap. Geol. Soc. Am.* **1993**, *284*, 21–40.
11. Nesbitt, H.W.; Young, G.M. Early Proterozoic climates and plate motions inferred from major element chemistry of lutites. *Nature* **1982**, *299*, 715–717. [[CrossRef](#)]
12. Armstrong-Altrin, J.S. Evaluation of two multidimensional discrimination diagrams from beach and deep-sea sediments from the Gulf of Mexico and their application to Precambrian clastic sedimentary rocks. *Int. Geol. Rev.* **2015**, *57*, 1446–1461. [[CrossRef](#)]
13. Chen, G.; Robertson, A.H.F. User’s guide to the interpretation of sandstones using whole-rock chemical data, exemplified by sandstones from Triassic to Miocene passive and active margin settings from the Southern Neotethys in Cyprus. *Sediment. Geol.* **2020**, *400*, 105616. [[CrossRef](#)]
14. Sallam, E.S.; Wanas, H.A. Petrography and geochemistry of the Jurassic siliciclastic rocks in the Khashm El-Galala area (NW Gulf of Suez, Egypt): Implication for provenance, tectonic setting and source area paleoweathering. *J. Afr. Earth Sci.* **2019**, *160*, 103607. [[CrossRef](#)]
15. Pourdivanbeigi Moghaddam, S.; Salehi, M.A.; Jafarzadeh, M.; Zohdi, A. Provenance, palaeoweathering and tectonic setting of the Ediacaran Bayandor Formation in NW Iran: Implications for the northern Gondwana continental margin during the late Neoproterozoic. *J. Afr. Earth Sci.* **2020**, *161*, 103670. [[CrossRef](#)]
16. Zhu, Q.; Li, J.; Wen, S.; Li, G.; Yu, R.; Miao, P.; Zhang, B. Alteration, uranium occurrence state, and enrichment mechanism of the Cretaceous Luohe Formation, southwestern Ordos Basin, western China. *Ore Geol. Rev.* **2021**, *139*, 104486. [[CrossRef](#)]
17. Yue, L.; Jiao, Y.; Fayek, M.; Wu, L.; Rong, H. Micromorphologies and sulfur isotopic compositions of pyrite in sandstone-hosted uranium deposits: A review and implications for ore genesis. *Ore Geol. Rev.* **2021**, *139*, 104512. [[CrossRef](#)]
18. Zhu, Q.; Yu, R.; Feng, X.; Li, J.; Sima, X.; Tang, C.; Xu, Z.; Liu, X.; Si, Q.; Li, G.; et al. Mineralogy, geochemistry, and fluid action process of uranium deposits in the Zhiluo Formation, Ordos Basin, China. *Ore Geol. Rev.* **2019**, *111*, 102984. [[CrossRef](#)]
19. Chen, L.; Chen, Y.; Feng, X.; Li, J.G.; Guo, H.; Miao, P.; Jin, R.; Tang, C.; Zhao, H.; Wang, G.; et al. Uranium occurrence state in the Tarangaole area of the Ordos Basin, China: Implications for enrichment and mineralization. *Ore Geol. Rev.* **2019**, *115*, 103034. [[CrossRef](#)]
20. Cai, Y.; Han, M.; Zhang, C.; Chao, Y.I.; Xiaocui, L.I.; Zhang, Y.; Wang, G.; Huaming, L.I. Geological and Geochemical Characteristics of the Zhiluo Formation in the Bayinqingeli Uranium Deposit, Northern Ordos Basin: Significance for Uranium Mineralization. *Acta Geol. Sin.* **2021**, *95*, 2075–2086. [[CrossRef](#)]
21. Tao, Z.; Jiao, Y.; Wu, L.; Rong, H.; Zhang, F.; Yue, L. Architecture of a sandstone uranium reservoir and the spatial distribution of its internal carbonaceous debris: A case study of the Zhiluo Formation, eastern Ordos Basin, Northern China. *J. Asian Earth Sci.* **2020**, *191*, 104219. [[CrossRef](#)]
22. Tao, R.; Shu, X.; Hai, L.; Guo, P.; Lin, L.; Tian, J.; Xu, Q.; Wang, L. Significance of sandstone provenance in tracking potential uranium reservoirs: A case study of the Middle Jurassic Zhiluo Formation, western Ordos Basin, northern China. *J. Asian Earth Sci.* **2022**, *227*, 105117. [[CrossRef](#)]
23. Jin, R.S.; Feng, X.X.; Teng, X.M.; Nie, F.J.; Cao, H.Y.; Hou, H.Q.; Liu, H.X.; Miao, P.S.; Zhao, H.L.; Chen, L.L.; et al. Genesis of green sandstone/mudstone from Middle Jurassic Zhiluo Formation in the Dongsheng Uranium Orefield, Ordos Basin and its enlightenment for uranium mineralization. *China Geol.* **2020**, *3*, 52–66. [[CrossRef](#)]
24. Zhu, Q.; Li, J.; Li, G.; Wen, S.; Yu, R.; Tang, C.; Feng, X.; Liu, X. Characteristics of sandstone-type uranium mineralization in the Hangjinqi region of the northeastern Ordos Basin: Clues from clay mineral studies. *Ore Geol. Rev.* **2022**, *141*, 104642. [[CrossRef](#)]
25. Yu, R.A.; Wang, S.B.; Zhu, Q.; Si, Q.H.; Teng, X.M.; Liu, X.X.; Liu, H.N.; Tang, Y.X. Zircon U-Pb ages and provenance characteristics of the Zhiluo Formation sandstones and the formation background of the uranium deposit in Huangling area, Ordos Basin, China. *China Geol.* **2021**, *4*, 600–615. [[CrossRef](#)]
26. Mathew, S.; Karmakar, P.; Bidwai, R.; Sharma, S.K.; Goyal, N.; Sinha, D.K. Provenance and depositional characteristics of Lathi Formation in southern part of Jaisalmer Basin: Implications for exploration of sandstone type uranium mineralization. *J. Indian Assoc. Sedimentol.* **2021**, *38*, 41–50. [[CrossRef](#)]
27. Zaid, S.M. Provenance, diagenesis, tectonic setting and geochemistry of Rudies sandstone (Lower Miocene), Warda Field, Gulf of Suez, Egypt. *J. Afr. Earth Sci.* **2012**, *66–67*, 56–71. [[CrossRef](#)]
28. Chen, R.; Wang, F.; Li, Z.; Evans, N.J.; Chen, H.; Wei, X. Late Paleozoic provenance shift in the east-central Ordos Basin: Implications for the tectonic evolution of the north China Craton. *J. Asian Earth Sci.* **2021**, *215*, 104799. [[CrossRef](#)]
29. Cox, R.; Lowe, D.R.; Cullers, R.L. The influence of sediment recycling and basement composition on evolution of mudrock chemistry in the southwestern United States. *Geochim. Cosmochim. Acta* **1995**, *59*, 2919–2940. [[CrossRef](#)]
30. Fedo, C.M.; Nesbitt, H.W.; Young, G.M. Unravelling the effects of potassium metasomatism in sedimentary rocks and paleosols, with implications for paleoweathering conditions and provenance. *Geology* **1995**, *23*, 921–924. [[CrossRef](#)]

31. Tchouatcha, M.S.; Azinwi Tamfuh, P.; Sobdjou, C.K.; Mbese, C.O.; Ngnotue, T. Provenance, palaeoweathering and depositional environment of the cretaceous deposits from the Babouri-Figuil and Mayo Oulo-Lere basins (North-Cameroon) during the Southern Atlantic opening: Geochemical constraints. *J. Afr. Earth Sci.* **2021**, *174*, 104052. [\[CrossRef\]](#)
32. Herron, M.M. Geochemical classification of terrigenous sands and shales from core or log data. *J. Sediment. Petrol.* **1988**, *58*, 820–829. [\[CrossRef\]](#)
33. Rudnick, R.L.; Gao, S. Composition of the continental crust. In *Treatise on Geochemistry*; Elsevier Science: Amsterdam, The Netherlands, 2003; pp. 1–64.
34. Taylor, S.R.; McLennan, S.M. *The Continental Crust: Its Composition and Evolution. An Examination of the Geochemical Record Preserved in Sedimentary Rocks*; Blackwell Scientific Pu: Oxford, UK, 1985.
35. Morton, A.C.; Hallsworth, C.R. Processes controlling the composition of heavy mineral assemblages in sandstones. *Sediment. Geol.* **1999**, *124*, 3–29. [\[CrossRef\]](#)
36. Roser, B.P.; Korsch, R.J. Determination of tectonic setting of sandstone-mudstone suites using SiO₂ content and K₂O/Na₂O ratio. *J. Geol.* **1986**, *94*, 515–533. [\[CrossRef\]](#)
37. Adepoju, S.A.; Ojo, O.J.; Akande, S.O.; Sreenivas, B. Petrographic and geochemical constraints on petrofacies, provenance and tectonic setting of the upper cretaceous sandstones, Northern Bida Basin, north-central Nigeria. *J. Afr. Earth Sci.* **2021**, *174*, 104041. [\[CrossRef\]](#)
38. Roser, B.P.; Korsch, R.J. Provenance signatures of sandstone-mudstone suites determined using discriminant function analysis of major-element data. *Chem. Geol.* **1988**, *67*, 119–139. [\[CrossRef\]](#)
39. Hayashi, K.I.; Fujisawa, H.; Holland, H.D.; Ohmoto, H. Geochemistry of ~1.9 Ga sedimentary rocks from northeastern Labrador, Canada. *Geochim. Cosmochim. Acta* **1997**, *61*, 4115–4137. [\[CrossRef\]](#)
40. Hans Wedepohl, K. The composition of the continental crust. *Geochim. Cosmochim. Acta* **1995**, *59*, 1217–1232. [\[CrossRef\]](#)
41. Verma, S.P.; Armstrong-Altrin, J.S. Geochemical discrimination of siliciclastic sediments from active and passive margin settings. *Sediment. Geol.* **2016**, *332*, 1–12. [\[CrossRef\]](#)
42. Floyd, P.A.; Leveridge, B.E. Tectonic environment of the Devonian Gramscatho basin, south Cornwall: Framework mode and geochemical evidence from turbiditic sandstones (England). *J. Geol. Soc.* **1987**, *144*, 531–542. [\[CrossRef\]](#)
43. Floyd, P.A.; Winchester, J.A.; Park, R.G. Geochemistry and tectonic setting of Lewisian clastic metasediments from the Early Proterozoic Loch Maree Group of Gairloch, NW Scotland. *Precambrian Res.* **1989**, *45*, 203–214. [\[CrossRef\]](#)
44. Bhatia, M.R.; Crook, K.A.W. Trace element characteristics of graywackes and tectonic setting discrimination of sedimentary basins. *Contrib. Mineral. Petrol.* **1986**, *92*, 181–193. [\[CrossRef\]](#)
45. Condie, K.C.; Wronkiewicz, D.J. The Cr/Th ratio in Precambrian pelites from the Kaapvaal Craton as an index of craton evolution. *Earth Planet. Sci. Lett.* **1990**, *97*, 256–267. [\[CrossRef\]](#)
46. Bracciali, L.; Marroni, M.; Pandolfi, L.; Rocchi, S. Geochemistry and petrography of Western Tethys Cretaceous sedimentary covers (Corsica and Northern Apennines): From source areas to configuration of margins. *Spec. Pap. Geol. Soc. Am.* **2007**, *420*, 73–93. [\[CrossRef\]](#)
47. Verma, S.P.; Armstrong-Altrin, J.S. New multi-dimensional diagrams for tectonic discrimination of siliciclastic sediments and their application to Precambrian basins. *Chem. Geol.* **2013**, *355*, 117–133. [\[CrossRef\]](#)
48. McLennan, S.M. Composition of the Upper Continental Crust Revisited: Insights from Sedimentary Rocks. *Mineral. Mag.* **1998**, *62A*, 983–984. [\[CrossRef\]](#)
49. Wronkiewicz, D.J.; Condie, K.C. Geochemistry of Archean shales from the Witwatersrand Supergroup, South Africa: Source-area weathering and provenance. *Geochim. Cosmochim. Acta* **1987**, *51*, 2401–2416. [\[CrossRef\]](#)
50. Cullers, R.L.; Podkovyrov, V.N. Geochemistry of the Mesoproterozoic Lakhanda shales in southeastern Yakutia, Russia: Implications for mineralogical and provenance control, and recycling. *Precambrian Res.* **2000**, *104*, 77–93. [\[CrossRef\]](#)
51. Kroonenberg, S.B. Effect of provenance, sorting and weathering on the geochemistry of fluvial sands from different tectonic and climatic environments. In Proceedings of the 29th International Geological Congress, Part A, Kyoto, Japan, 24 August–3 September 1992; Volume 69, p. 81.
52. Maynard, J.B.; Valloni, R.; Yu, H.S. Composition of modern deep-sea sands from arc-related basins. *Geol. Soc. Spec. Publ.* **1982**, *10*, 551–561. [\[CrossRef\]](#)
53. Wanas, H.A.; Assal, E.M. Provenance, tectonic setting and source area-paleoweathering of sandstones of the Bahariya Formation in the Bahariya Oasis, Egypt: An implication to paleoclimate and paleogeography of the southern Neo-Tethys region during Early Cenomanian. *Sediment. Geol.* **2021**, *413*, 105822. [\[CrossRef\]](#)
54. Bhatia, M.R. Rare earth element geochemistry of Australian Paleozoic graywackes and mudrocks: Provenance and tectonic control. *Sediment. Geol.* **1985**, *45*, 97–113. [\[CrossRef\]](#)
55. Whalen, J.B.; Currie, K.L.; Chappell, B.W. A-type granites: Geochemical characteristics, discrimination and petrogenesis. *Contrib. Mineral. Petrol.* **1987**, *95*, 407–419. [\[CrossRef\]](#)
56. Ge, X.; Mou, C.; Yu, Q.; Liu, W.; Men, X.; He, J. The geochemistry of the sedimentary rocks from the Huadi No. 1 well in the Wufeng-Longmaxi formations (Upper Ordovician-Lower Silurian), South China, with implications for paleoweathering, provenance, tectonic setting and paleoclimate. *Mar. Pet. Geol.* **2019**, *103*, 646–660. [\[CrossRef\]](#)